# Generalized Scaling on Forecasting Heating Patterns for Microwave Processing

**Madhuchhanda Bhattacharya**
D29-81 Adyar Avenue, Indian Institute of Technology Madras, Chennai - 600 036, India

**Tanmay Basak**
Dept. of Chemical Engineering, Indian Institute of Technology Madras, Chennai - 600036, India

*DOI 10.1002/aic.11341*
*Published online December 4, 2007 in Wiley InterScience (www.interscience.wiley.com).*

*A closed form analysis based on Finite Fourier Transformation (FFT) has been carried out to predict the heating characteristics in the presence of microwave induced volumetric heat sources. A scaling analysis shows that temperature distributions within a material during microwave heating evolve in two stages, namely small time and large time. The inverse of square of second eigenvalue along with thermal diffusivity determines the threshold time scale between these two regimes. During small time evolution, the spatial temperature distribution follows absorbed power profiles, whereas the temperature distributions are slaved by first eigenfunction and independent of volumetric heat distribution at large time evolution. In all the cases, the variation of temperature within the material is guided by a dimensionless number* $N_G = L^2 q_0/kT_{ref}$. *For* $N_G \ll 1$, *almost uniform temperature distributions are attained and a lump parameter model can be used. In contrast, nonuniformity in absorbed power distributions amplifies in temperature distribution for materials with* $N_G \gg 1$, *where there exists a possibility of local hot spot formation if absorbed power exhibits local maxima. The applicability of this analysis has been illustrated to forecast heating characteristics within various materials*
 *AIChE J,* 54: 56–73, 2008
*Keywords:* microwave heating, modeling, analytical solution, Finite Fourier Transformation

## Introduction

Microwave radiations within frequency range 300 MHz–300 GHz are commonly used for material processing due to their ability to generate volumetric heat sources.[1–5] Volumetric heating results in enhanced processing rate and various applications, based on microwave radiations have been reported by earlier researchers. A number of experimental, as well as theoretical/numerical studies have been carried out for microwave heating, thawing, drying, material processing etc.[1–13] Ayappa et al.[1,2] carried out theoretical and numerical studies of microwave power and temperature dynamics in presence of uniform plane wave. The numerical predictions of temperature within one and two-dimensional (2-D) samples were obtained using finite element method (FEM). Further, FEM has also been used by Basak and Ayappa[5] and Bhattacharya et al.[6] for microwave thawing of 1-D samples in the presence of uniform plane wave. Liu et al.[7] carried out theoretical studies on evaluation of microwave power in lossy dielectric materials within 3-D cavities. They obtained electric and magnetic fields using finite difference time domain (FDTD) algorithm. Later Liu et al.[8] extended FDTD algorithm to evaluate power and temperature within polymeric materials inside a ridge waveguide. FDTD method was further used by Zhang et al.[9,10] for analyzing microwave heating of tissues and natural convection within 3-D waveguides.

Correspondence concerning this article should be addressed to T. Basak at tanmay@iitm.ac.in.

Ratanadecho et al.[3,4] analyzed microwave drying and melting of samples within 3-D wave guides using FDTD algorithm.

A few experimental and numerical comparisons on microwave heating and thawing of cylindrical samples have been reported by earlier researchers.[11–13] Their numerical predictions agreed well with the experimental observations. However, all the comparisons were restricted to Lambert's law, where power is assumed to decay exponentially from the surface. This assumption is valid for thick samples and may not be appropriate for thinner samples, where a proper representation of microwave power based on detail solution of Helmholtz equation is necessary. Although the numerical predictions agreed well with experimental data for thick samples, those numerical models may not be appropriate for predicting the local maxima on microwave power or hot spots.

The volumetric heat generation is mainly due to spatial power absorption, based on the interference between traveling waves, namely transmitted and reflected waves. The interference between traveling waves leads to spatial maxima or resonances in absorbed power, which results in localized higher heating rates within the material as discussed by earlier researchers.[14–18] Spatially nonuniform volumetric heating results in spatial gradients in temperature profiles, and in turn may initiate localized hot spots within the material during exposure to microwave radiations. The localized hot spots may not be desirable for certain applications e.g., food processing since they in turn degrade the final quality of material.

Significant amount of previous works on hot spot formation form the basis of the present analysis on spatial heating characteristics due to microwaves. Marchant and Pincombe[19] studied microwave heating of 1-D slab with temperature dependent material properties, and reported an asymptotic solution for power law dependent material properties. This solution was compared with the numerical solution and used to verify localized hot spot formation. Later, this study was extended to the formation of hot spots in the presence of impurities,[20] and the steady-state solutions within a parameter space was analyzed. Andonowati and Chandra[21] studied steady-state microwave heating of a unit slab of three layers of materials with different thermal conductivities. An eigenfunction expansion for the problem based on Galerkin method was described and fundamental-mode approximation was presented in their study. They observed that the position of the inner layer with low thermal conductivity is related to the hot spot formation. Ward[22] studied microwave heating of thin cylindrical samples, and their study concluded that the hot spot depends on a competition between the maxima of the electric field and the maximum deformation of circular cylinder. Reimbert et al.[23] studied localized hot spots via a simple analytic expression.

A number of investigations on thermal runaway leading to hot spots were also reported in various applications. Yang and Gunasekaran[24] have carried out numerical investigations of cylindrical food samples with pulsed and continuous microwave incidence. They observed a local hot spot at the center portion of the sample during continuous microwave heating, while the hot spot was less significant for pulsed microwave heating. Vriezinga et al.[25] studied thermal runaway and analyzed multiple steady-state solutions. Thermal runaway during microwave thawing was also analyzed by earlier researchers.[26,27] Recently, spatial maxima in temperature has been reported[28,29] for samples supported on ceramic and/or metallic supports at the resonant situation. Common to all these studies is extensive numerical investigations on hot spot formation, which found the hot spots in microwave heating to be driven by spatial nonuniformities of absorbed power.

Extensive research on occurrence of hot spots during microwave heating lead to several questions: Does always local maxima in spatial power distribution result in localized hot spots in temperature distributions? When temperature distributions are slaved by absorbed power profiles? Is the dependency of temperature distributions on absorbed power distributions time invariant? What are the parameters that drive the formation of local hot spots? Are there any generalized material invariant characteristics or scaling to obtain the conditions for hot spots? A comprehensive concept on scaling for heat transfer due to conduction and convection was first proposed by Bejan[30]; however, those scalings are useful for heat-transfer processes mainly in absence of volumetric heat sources. Hence, a closed form analysis of temperature distributions due to microwave heating may be necessary to address the previous issues, and such a closed form analysis is yet to appear in the literature.

The closed form solution of microwave power with detailed analysis on asymptotes and resonances have been reported recently by Bhattacharya and Basak.[31,32] These works[31,32] are mainly devoted on the derivation and analysis of closed form solution for absorbed power distributions. These works established various regimes of microwave power absorption and derived closed form relationships for the corresponding sample lengths. Initiation of hot spots due to local maxima in absorbed power distributions was illustrated in reference[32] via "numerical solution" of energy balance equations for few specific materials. This work illustrates the temperature distributions at few specified conditions in order to show the correspondence between hot spots and absorbed power distributions. However, the effect of thermal parameters on temperature distributions over the entire parameter space could not be illustrated in the cited references due to limitations of numerical solutions. In addition, various characteristics of temperature distributions could not be quantified due to lack of analytical solution.

The prime objective of the present manuscript is to quantify various characteristics of temperature distributions over the entire parameter space. In particular, the focus of the current manuscript is on material invariant time scales associated with microwave heating and their influences on heating patterns. Numerical solutions can give estimates for specific conditions, and, thus, cannot be used to establish a generalized time scales or heating patterns. Therefore, there is a need to obtain a closed form solution of the energy balance equation in the presence of volumetric heat generation due to microwave power. In order to analyze various time scales, the eigenfunctions are needed as a part of entire solution procedure and Finite Fourier Transformation (FFT) can be suitably used as discussed in Appendix B.

In this article, the energy balance equation with volumetric heat generation has been solved using FFT. A detailed analysis on the closed form solution has been performed to establish the relationship between temperature distributions and imposed internal heat source profiles. The two key issues on "spatial temperature profile" vs "uniform heating" have

been analyzed using eigenvalues and eigenfunctions of the operator. Several applications have also been demonstrated to establish heating characteristics in various materials.

### *Governing equations for microwave heating*

Let us consider a semiinfinite slab of length $2L$ exposed to uniform plane microwave radiations of intensities $I_L$ and $I_R$ from left and right sides, respectively (see Figure 1). The slab is initially maintained at temperature $T_0$. Depending on dielectric properties and length of the slab, and also on the distribution of $I_L$ and $I_R$, microwaves induce volumetric heat sources denoted by $q(z')$, and cause heating effects within the slab (details of microwave power absorption given in Appendix A). Assuming constant density ($\rho$), heat capacity ($C_p$) and thermal conductivity ($k$), evolution of temperature within the slab during exposure to microwave radiations can be determined from the following equation

$$\rho C_p \frac{\partial T}{\partial t} = k\frac{\partial^2 T}{dz'^2} + q(z'), \quad -L \le z' \le L \tag{1a}$$

$$k\frac{\partial T}{\partial z'} = h_L(T - T_\infty) \quad @\ z' = -L \tag{1b}$$

$$-k\frac{\partial T}{\partial z'} = h_R(T - T_\infty) \quad @\ z' = L \tag{1c}$$

Equations 1b and 1c account for heat loss to ambient, where $T_\infty$ is the ambient temperature and $h_L$ and $h_R$ are left and right side heat-transfer coefficients, respectively. Note that, the use of different heat-transfer coefficients for left and right sides are convenient for adopting the cases of either one side thermally insulated (either $h_L$ or $h_R = 0$), or one side fixed at constant temperature (either $h_L$ or $h_R \to \infty$).

Defining

$$\theta = \frac{T}{T_\infty}, \quad \theta_0 = \frac{T_0}{T_\infty}, \quad \tau = \frac{t}{\alpha}, \quad z = \frac{z'}{L}, \quad p(z) = \frac{q(z'/L)}{q_0},$$
$$\{Bi_l\}_{l=L,R} = \frac{h_l L}{k}, \quad N_G = \frac{q_0 L^2}{kT_\infty}, \tag{2}$$

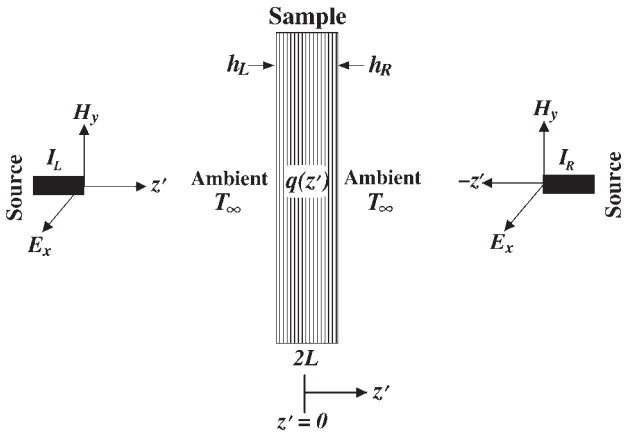


**Figure 1. Representation of a 1-D sample with internal heat source $p(z)$ due to absorption of microwave from left and right sides.**

where $\alpha = \rho C_p L^2/k$ is the thermal diffusion time, $q_0 = I_0/L$ with $\sqrt{I_0} = \sqrt{I_L} + \sqrt{I_R}$ is the characteristic volumetric heat source, and $Bi_L$ and $Bi_R$ are left and right side Biot numbers, respectively, dimensionless form of Eq. 1 can be written as

$$\frac{\partial \theta}{\partial \tau} = \frac{\partial^2 \theta}{\partial z^2} + N_G p(z), \quad -1 \le z \le 1 \tag{3a}$$

$$\frac{\partial \theta}{\partial z} = Bi_L(\theta - 1) \quad @\ z = -1 \tag{3b}$$

$$-\frac{\partial \theta}{\partial z} = Bi_R(\theta - 1) \quad @\ z = 1 \tag{3c}$$

$$\theta = \theta_0 \quad @\ \tau = 0 \tag{3d}$$

In Eq. 3a, $p(z)$ is the dimensionless absorbed power distribution, whose dependency on various microwave related parameters can be expressed in terms of wave number ($N_w$), penetration number ($N_p$), wave number of free space ($N_{w,0}$), and the fractional incident electric field from the left side ($\phi_0$), and is given in Appendix A (see Eq. A6).

Using Finite Fourier Transformation as discussed in Appendix B, analytical solution of Eq. 3 is obtained as

$$\theta = 1 + \sum_{n=1}^{\infty}\left[\langle 1, \psi_n(z)\rangle(\theta_0 - 1)e^{-\mu_n^2\tau} + N_G\frac{1 - e^{-\mu_n^2\tau}}{\mu_n^2}p_n\right]\psi_n(z) \tag{4}$$

where $\mu_n$ and $\psi_n(z)$ are $n$th eigenvalue and eigenfunction, respectively, associated with Eq. B2. The closure $p_n$ in Eq. 4 is the power Fourier coefficient, which is defined as

$$p_n = \langle p(z), \psi_n(z)\rangle \tag{5}$$

and the closed form expression for $p_n$ is given in Eq. B7b (see Appendix B for details). In Eq. 4, the first term within the bracket represents thermal diffusion due to different initial and ambient temperatures, while the second term corresponds to thermal diffusion due to imposed internal heat sources. Therefore, depending on the relative magnitude of the two terms, which not only depend on $|\theta_0 - 1|$ and $N_G$, but also depend on $\tau$, either of these two may play a significant role on temperature distribution within the slab. Since the main focus of this work is to identify the heating characteristics due to microwave induced internal heat sources, $\theta_0 = 1$ will be assumed throughout the work in order to minimize external effects.

### *Various distributions of microwave induced volumetric heat sources*

It may be noted from Eq. A6 that $p(z)$ has exponential, as well as sinusoidal position dependencies and relative magnitudes of the two depend primarily on $N_p = 2L/D_p$. Thus, microwave induced volumetric heat source may follow either exponential or sinusoidal distributions depending on the absolute magnitude of $N_p$. For example, $p(z)$ follows exponential distributions for $N_p \gg 1$, where exponential terms dominate over sinusoidal one. This regime will be referred to as exponential regime. On the other hand, $p(z)$ exhibits spatial oscillations following the sine functions of Eq. A6 for $N_p \not\gg 1$, where exponential functions do not dominate over the

Table 1. Thermal and Dielectric Properties of Marinated Shrimp,[33] Potato,[34] Bread[35] and Alumina[17]

| Material Property | Potato (3000 MHz) | Bread (2800 MHz) | Shrimp (2450 MHz) | Alumina (2450 MHz) |
|---|---|---|---|---|
| Dielectric constant, $\kappa'$ | 57.3 | 4.6 | 61.4 | 10.8 |
| Dielectric loss, $\kappa''$ | 15.7 | 0.6 | 31.4 | 0.1566 |
| Wavelength, $\lambda_m$ (cm) | 1.31 | 4.98 | 1.52 | 3.72 |
| Penetration depth, $D_p$ (cm) | 1.55 | 12.21 | 1.00 | 81.74 |
| Heat capacity, $C_p$ (J kg$^{-1}$ K$^{-1}$) | 3517 | 2850 | 1069 | 1046 |
| Thermal conductivity, $k$ (W m$^{-1}$ K$^{-1}$) | 0.554 | 0.45 | 0.47 | 26 |
| Density, $\rho$ (kg m$^{-3}$) | 1090 | 800 | 2500 | 3750 |

sinusoidal one.[17,31,32] This regime will be referred to as sinusoidal regime, where the frequency of spatial oscillations is proportional to $N_w$. Thus, $N_w$ and $N_p$ are the characteristic length scales in sinusoidal and exponential regimes, respectively, and the following discussion on power distributions will be based on $N_w = 2L/\lambda_m$ and $N_p$.

In this work, we will consider potato, bread, shrimp and Alumina, which are of interest for various food/material processing. Thermal and dielectric properties of these materials are listed in Table 1, where dielectric properties are reported at 2,450 MHz for shrimp and Alumina, at 3,000 MHz for potato, and at 2,800 MHz for bread. The same frequency of microwave radiations will be used for rest of the discussions. It may be noted from Table 1 that penetration depths of Alumina and bread are much higher than those of potato and shrimp with shrimp having the smallest penetration depth. Consequently, the critical sample length at the transition between sinusoidal and exponential regimes, which is proportional to $D_p$, is much higher for Alumina and decreases with bread, potato and shrimp. On the other hand, potato has smallest wavelength and exhibits higher frequency of spatial oscillations in sinusoidal regime compared to other materials of same length. These characteristics will be illustrated below for various distributions of $I_L$ and $I_R$ as $\phi_0 = 0$, 1/4 and 1/2. In all the illustrations, total incident electric field is assumed to be constant at $E_0 = (2I_0/c\varepsilon_0)^{1/2}$ with $I_0 = 3$ W cm$^{-2}$.

As mentioned in Appendix A, $0 \le \phi_0 \le 1$ is a measure of fractional intensity of microwave radiations from left side. $\phi_0 = 0$ and 1 correspond to one side incidence, while $\phi_0 = 1/2$ represents equal intensity of microwave radiations from both the sides. Any intermediate $\phi_0$ corresponds to uneven microwave incidences from left and right sides. Therefore, as $\phi_0$ approaches 1/2 from either 0 or 1 with constant total incident electric field, the source of microwave radiations is distributed from one side to both side with various combination of incident intensities from left and right sides. As $p(z)|_{\phi_0} = p(-z)|_{1-\phi_0}$, $\phi_0 = 0$, 1/4 and 1/2 illustrate the effect of distri-

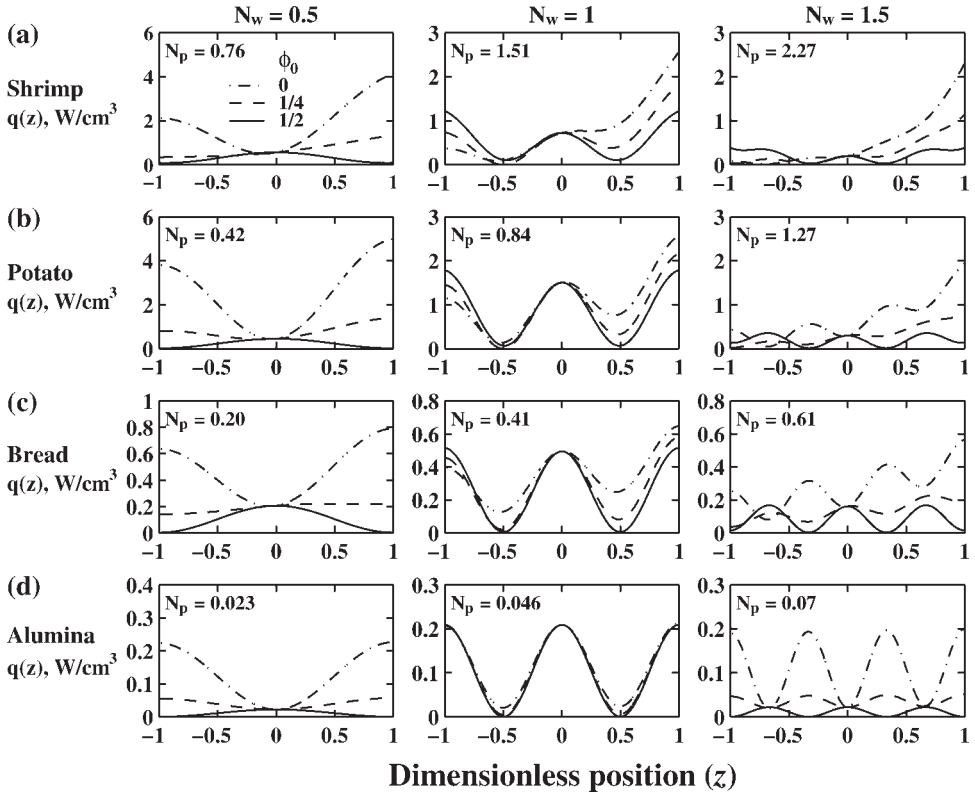


**Figure 2. Sinusoidal distributions of absorbed power in shrimp, potato, bread and Alumina for $N_w = 0.5$, 1 and 1.5, $\phi_0 = 0$ (dashed-dotted lines), 1/4 (dashed lines) and 1/2 (solid lines).**

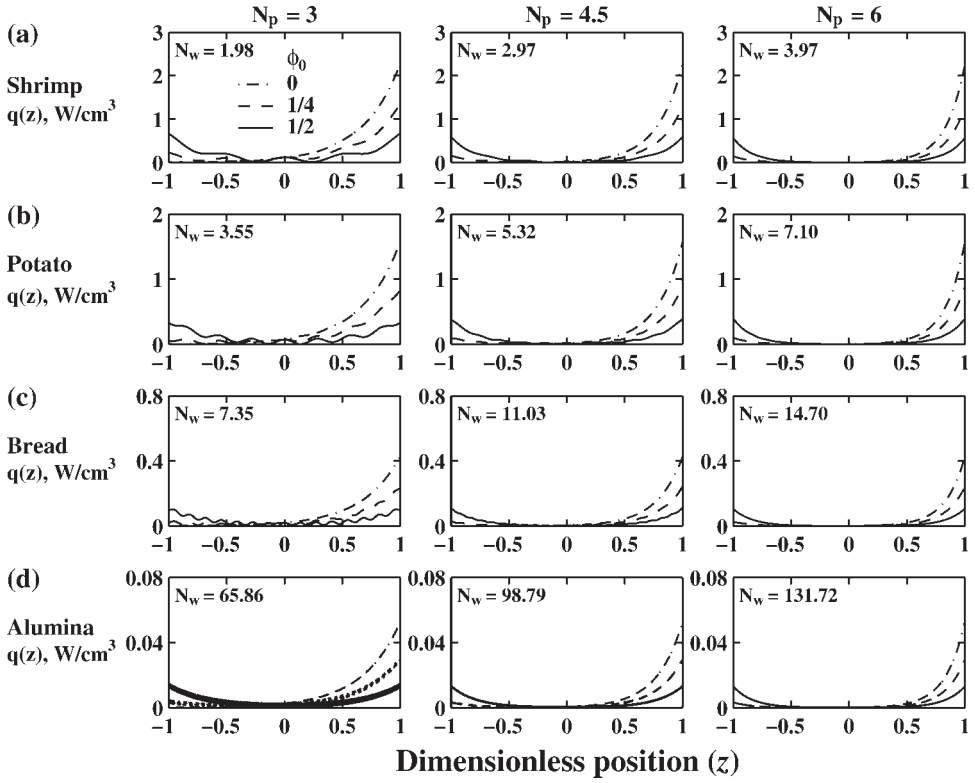


**Figure 3. Exponential distributions of absorbed power in shrimp, potato, bread and Alumina for $N_p$ = 3, 4.5 and 6, $\phi_0$ = 0 (dashed-dotted lines), 1/4 (dashed lines) and 1/2 (solid lines).**

bution of microwave source over the entire spectra of one side to both side incidence. In other words, $p(z)|_{1/2 \le \phi_0 \le 1}$ are mirror reflections of $p(z)|_{1/2 \ge \phi_0 \ge 0}$, respectively, and will not be shown in any of the illustrations.

Figure 2 illustrates absorbed power distributions in sinusoidal regime for $N_w$ = 0.5, 1 and 1.5. Corresponding $N_p$'s, which can be calculated from $\lambda_m$ and $D_p$ values listed in Table 1, are reported in each subplot. It may be noted that maximum value of $N_p$ associated with Figure 2 is within sinusoidal regime, and, consequently, absorbed power exhibits oscillations of frequency $N_w$ following the sinusoidal function of Eq. A6 for all the four materials. However, the oscillations of $p(z)$ are much more prominent in Alumina and reduces with bread, potato and shrimp in order. This is due to the fact that for any fixed $N_w$, $N_p$ is directly proportional to $\lambda_m/D_p$, which is in ascending order from Alumina to bread, potato and shrimp (see Table 1). Thus, higher contributions from exponential terms of Eq. A6 compared to the sinusoidal ones for materials with higher $\lambda_m/D_p$ cause respective attenuation of oscillations in $q(z)$ as observed in Figure 2. It may also be noted from Figure 2 that attenuation of oscillations also increase with increasing $N_w$, due to a corresponding increase in $N_p$. Higher $\lambda_m/D_p$ for shrimp compared to other materials also results in higher relative increase in $N_p$ as $N_w$ increase from 0.5 to 1 or 1.5 and cause higher attenuation of the oscillations within shrimp as can be seen from Figure 2. Thus, shrimp reaches exponential regime at much lower sample length (or $N_w$) compared to the other materials as shown in Figure 3.

In the exponential regime, sample length is much higher than penetration depth and absorbed power distributions attenuate completely within the material as shown in Figure 3 for $N_p$ = 3, 4.5 and 6. However, it may be noted that the critical $N_p$, which is the minimum sample length to penetration depth ratio required to reach the exponential regime, depends strongly on $\phi_0$. For one side incidence, $q(z)$ exhibits exponential distributions for $N_p \ge 3$, whereas $N_p \ge 6$ is required to reach exponential regime for $\phi_0$ = 1/2. Critical $N_p$ for any intermediate $\phi_0$ lies within 3 to 6 as shown in Figure 3 for $\phi_0$ = 1/4. Therefore, the threshold boundary of the sample length required to reach exponential regime increases from three times to six times of penetration depth as microwave source is distributed from one side to both side.

It may be noted from Figure 3 that absorption of microwave radiations in exponential regime always starts from the exposed face (one side), or faces (both side), and penetrates within the material. As a result, maximum power absorptions or hot spots always initiate from the boundary of the sample. On the other hand, locations of spatial maxima of absorbed power depend on $N_w$ and $\phi_0$ in the sinusoidal regime, and, consequently, hot spots may initiate either at boundary or inside the sample or at both the locations. It is also important to note that overall spatial gradient of absorbed power within the sample always decrease with distributions of microwave source in exponential regime, whereas it is a complex function of dielectric properties of the material in sinusoidal regime. Thus, various distributions of $I_L$ and $I_R$ can be judi-

Table 2. Magnitude of $b_n = (1 - e^{-\mu_n^2\tau})/\mu_n^2$ at Various Dimensionless Times in Terms of $1/\mu_2^2$ for Three Limiting Cases of Boundary Conditions Given By (1) $Bi_L = Bi_R = 10^{-3}$, (2) $Bi_L = 10^{-3}$, $Bi_R = 10^2$ and (3) $Bi_L = Bi_R = 10^2$

| | | | $\tau = \frac{0.1}{\mu_2^2}$ | $\tau = \frac{0.5}{\mu_2^2}$ | $\tau = \frac{0.8}{\mu_2^2}$ | $\tau = \frac{1}{\mu_2^2}$ | $\tau = \frac{2}{\mu_2^2}$ | $\tau = \frac{5}{\mu_2^2}$ | $\tau = \frac{10}{\mu_2^2}$ | |
|---|---|---|---|---|---|---|---|---|---|---|
| $\mu_1$ | 0.0316 | $b_1(\tau)$ | 0.0405 | 0.2025 | 0.3239 | 0.4049 | 0.8096 | 2.0227 | 4.0414 | $Bi_L = Bi_R = 10^{-3}$ |
| $\mu_2$ | 1.5714 | $b_2(\tau)$ | 0.0385 | 0.1593 | 0.2230 | 0.2560 | 0.3502 | 0.4022 | 0.4049 | |
| $\mu_3$ | 3.1420 | $b_3(\tau)$ | 0.0334 | 0.0876 | 0.0972 | 0.0994 | 0.1013 | 0.1013 | 0.1013 | |
| $\mu_4$ | 4.7126 | $b_4(\tau)$ | 0.0267 | 0.0445 | 0.0450 | 0.0450 | 0.0450 | 0.0450 | 0.0450 | |
| $\mu_5$ | 6.2833 | $b_5(\tau)$ | 0.0202 | 0.0253 | 0.0253 | 0.0253 | 0.0253 | 0.0253 | 0.0253 | |
| $\mu_1$ | 0.7821 | $b_1(\tau)$ | 0.0181 | 0.0885 | 0.1392 | 0.1712 | 0.3262 | 0.6976 | 1.0957 | $Bi_L = 10^{-3}$, $Bi_R = 10^2$ |
| $\mu_2$ | 2.3447 | $b_2(\tau)$ | 0.0173 | 0.0716 | 0.1002 | 0.1150 | 0.1573 | 0.1807 | 0.1819 | |
| $\mu_3$ | 3.9076 | $b_3(\tau)$ | 0.0159 | 0.0492 | 0.0584 | 0.0614 | 0.0652 | 0.0655 | 0.0655 | |
| $\mu_4$ | 5.4706 | $b_4(\tau)$ | 0.0140 | 0.0312 | 0.0330 | 0.0333 | 0.0334 | 0.0334 | 0.0334 | |
| $\mu_5$ | 7.0335 | $b_5(\tau)$ | 0.0120 | 0.0200 | 0.0202 | 0.0202 | 0.0202 | 0.0202 | 0.0202 | |
| $\mu_1$ | 1.5552 | $b_1(\tau)$ | 0.0102 | 0.0486 | 0.0749 | 0.0915 | 0.1627 | 0.2950 | 0.3795 | $Bi_L = Bi_R = 10^2$ |
| $\mu_2$ | 3.1105 | $b_2(\tau)$ | 0.0098 | 0.0407 | 0.0569 | 0.0653 | 0.0894 | 0.1027 | 0.1034 | |
| $\mu_3$ | 4.6658 | $b_3(\tau)$ | 0.0093 | 0.0310 | 0.0383 | 0.0411 | 0.0454 | 0.0459 | 0.0459 | |
| $\mu_4$ | 6.2211 | $b_4(\tau)$ | 0.0085 | 0.0223 | 0.0248 | 0.0254 | 0.0258 | 0.0258 | 0.0258 | |
| $\mu_5$ | 7.7764 | $b_5(\tau)$ | 0.0077 | 0.0164 | 0.0164 | 0.0165 | 0.0165 | 0.0165 | 0.0165 | |

ciously used in sinusoidal regime in order to tune the spatial nonuniformities of temperature. However, this needs *a priori* knowledge about the temperature distribution characteristics and their evolution with time.

Evolution of temperature distributions during microwave heating not only depend on spatial distributions of absorbed power, but also depends on thermal parameters. Depending on thermal parameters, temperature distributions may or may not follow absorbed power distributions, and, consequently, strengthen or weaken the probability of hot spot formation due to nonuniformity in $q(z)$. Role of various thermal parameters on the evolution of heating patterns will be discussed in the following sections for both sinusoidal and exponential regime.

## Temperature Distributions vs. Power Distributions

### *Short time vs. long time*

For $\theta_0 = 1$, the close form expression of temperature (Eq. 4) can be simplified to

$$\theta = 1 + N_G \sum_{n=1}^{\infty} \frac{1 - e^{-\mu_n^2\tau}}{\mu_n^2} p_n \psi_n(z) \tag{6a}$$

$$= 1 + N_G \frac{1 - e^{-\mu_1^2\tau}}{\mu_1^2} p_1 \psi_1(z) + N_G \sum_{n=2}^{\infty} \frac{1 - e^{-\mu_n^2\tau}}{\mu_n^2} p_n \psi_n(z) \tag{6b}$$

It is evident that spatial distributions of temperature can be expressed as combinations of eigenfunctions ($\psi_n(z)$), where the contribution from $n$th eigenfunction is determined by the Fourier coefficient $c_n = p_n(1 - e^{-\mu_n^2\tau})/\mu_n^2$. Thus, temperature distribution at any time depends on the relative magnitude of $c_n$, which in turn depends on eigenvalues ($\mu_n$), absorbed power distribution (via $p_n$) and time ($\tau$). It may be further noted that absorbed power distributions can also be expressed as combination of eigenfunctions as given below

$$p(z) = \sum_{n=1}^{\infty} p_n \psi_n(z) \tag{7}$$

Comparing Eqs. 6a and 7 it is evident that whether $\theta(z)$ follows $p(z)$ or not is determined by relative magnitude of $b_n \equiv (1 - e^{-\mu_n^2\tau})/\mu_n^2$, and temperature distributions follow the power distributions if all $b_n$'s contribute effectively.

It may be noted that $b_n$ is an increasing function of time, where relative increase of $b_n$ decreases with increasing $n$. Thus, lower order term, namely $b_1$, may dominate over other $b_n$'s ($n \geq 2$), once a threshold time denoted by $t_L$ (or $\tau_L$ in dimensionless unit) is reached. Since eigenvalues depend on boundary conditions, relative increase of $b_n$ with time, and, consequently, threshold time also depend on Biot number as shown in Table 2. Table 2 lists magnitudes of first five coefficients ($b_1 - b_5$) at various times along with corresponding eigenvalues for three limiting cases of boundary conditions given by (1) $Bi_L = Bi_R = 10^{-3}$, (2) $Bi_L = 10^{-3}$, $Bi_R = 10^2$, and (3) $Bi_L = Bi_R = 10^2$. Here, the eigenvalues for various Biot numbers are calculated as first five positive roots of Eq. B5. It may be noted that the threshold time is defined as the time scale, after which the second term of Eq. 6b dominates over the third term, which occurs if $\mu_n^2\tau \gg 1$ for $n \geq 2$. Since $\mu_n$ increases with $n$, threshold time is obtained as $\tau_L = 1/\mu_2^2$, which is evident from Table 2. Hence, the times at which $b_n$'s are reported in Table 2 have been selected as multiples of $1/\mu_2^2$, which clearly shows that $\tau_L = 1/\mu_2^2$.

During $\tau < 1/\mu_2^2$, all $b_n$'s contribute effectively, and temperature distributions follow the absorbed power distribution patterns except the boundary effects. This will be referred to as "small time", where imposed heat source profiles determine the temperature distribution patterns. During small time, thermal diffusion tends to homogenize the spatial oscillations of temperature distributions, while imposed heat sources influence to enforce them. As a result, overall temperature distributions during small time evolve with time, but are slaved by $p(z)$. At $\tau \gg \tau_L$, the second term in Eq. 6b dominates, which simplifies Eq. 6b to

$$\theta = 1 + N_G \frac{1 - e^{-\mu_1^2\tau}}{\mu_1^2} p_1 \psi_1(z) + N_G \sum_{n=2}^{\infty} \frac{p_n}{\mu_n^2} \psi_n(z) \tag{8}$$

In this case, temperature distributions follow the first eigenfunction if spatial variations of $\psi_1(z)$ are not negligible compared to higher-order eigenfunctions. This will be referred to as "large time" temperature distributions, where spatial patterns of $\theta(z)$ remain almost unchanged with time.

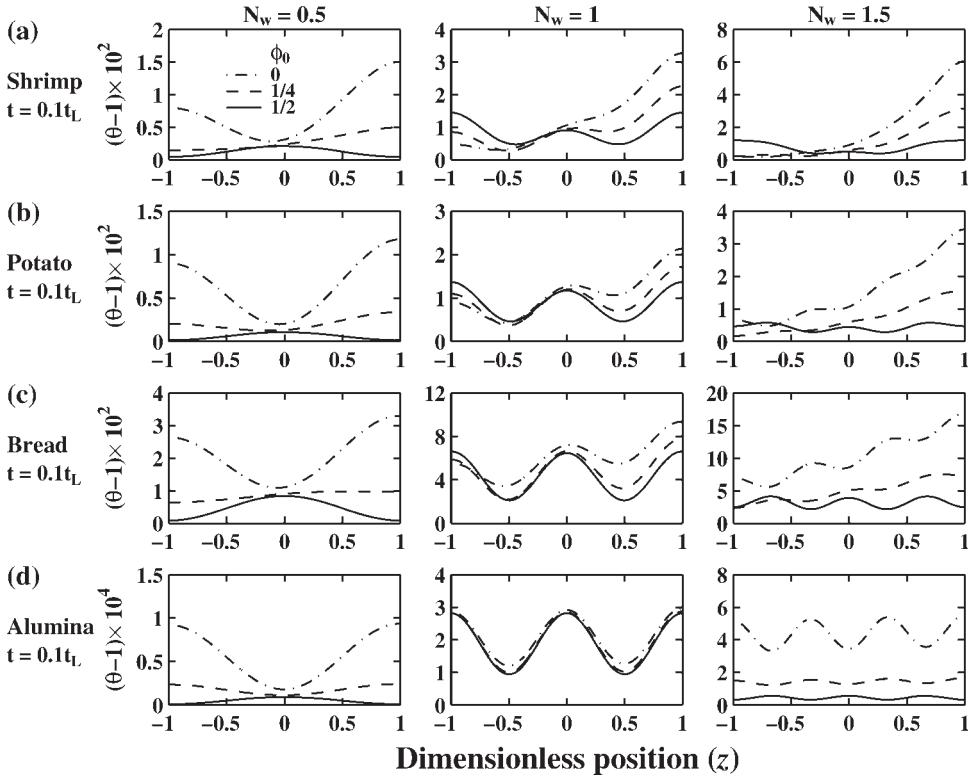


**Figure 4. Small time dimensionless temperature distributions in sinusoidal regime of microwave heating of shrimp, potato, bread and Alumina.**

The results correspond to $t = 0.1t_L$, $h_L = h_R = 2$ W m$^{-2}$ K$^{-1}$, $N_w = 0.5$, 1 and 1.5, $\phi_0 = 0$ (dashed-dotted lines), 1/4 (dashed lines) and 1/2 (solid lines).

Since, eigenfunctions are solely determined by Biot numbers, boundary conditions govern large time temperature distributions.

### *Distributed model vs lumped model*

It is evident from the previous discussion that temperature distributions within a material is governed by the time-dependent interactions between thermal diffusion and internal heat generation. The strength of thermal diffusion within a material is represented by $N_G$, which is the ratio of thermal diffusion time to that of characteristic internal heat generation time. Thus, $N_G$ represents the characteristic time required for a material to diffuse the imposed heat source profiles. For $N_G \ll 1$, the material can diffuse the heat much faster, and $\theta(z)$ quickly reaches uniform distribution. On the other hand, the temperature distributions exhibit nonuniformities following the absorbed power profiles for a longer period in materials with $N_G \gg 1$. $N_G$ also represents overall temperature gradients within the material as follows from Eq. 6a. Thus, materials with *higher $N_G$ are prone to hot spot formation* during microwave processing if $p(z)$ exhibits spatial nonuniformities. In this case, a distributed model given by Eq. 3 is necessary to determine the temperature distributions. Whereas, temperature distributions remain almost uniform for materials with $N_G \ll 1$, and a lump parameter model can be used to determine the evolution of temperature within the material. Integrating Eq. 3 with respect to $z$ and $\tau$, the lump parameter model is obtained as

$$\bar{\theta} = 1 + + \frac{2N_G\bar{p}}{Bi_L + Bi_R}\left(1 - e^{-\tau(Bi_L+Bi_R)/2}\right) \tag{9}$$

where, $\bar{\theta} = \frac{1}{2}\int_{-1}^{1}\theta(z)dz$ is the average temperature, and $\bar{p} = \frac{1}{2}\int_{-1}^{1}p(z)dz$ is average heat source.

It follows from the previous discussion that temperature distribution patterns during microwave heating evolve in two stages, where $\tau_L = 1/\mu_2^2$ or $t_L = \alpha/\mu_2^2$ draws the threshold boundary between the two. The threshold time depends on various thermal parameters, e.g., thermal conductivity, heat capacity (through $\alpha$) and heat-transfer coefficients (via $\mu_2$), in addition to sample length. Thus, heating patterns may either be confined within "small time" or may be extended to "large time", based on thermal parameters and sample length, which in turn determine $t_L$. The thermal parameters, namely $k$ and $L$, also determine overall temperature gradients within the material at any given intensity of radiation via $N_G$, and may initiate hot spots during microwave heating. The effects of these parameters on temperature distributions during both the stages of microwave heating will be illustrated for both sinusoidal and exponential regime of power distributions.

### *Illustrations*

*Small Time Temperature Distribution: Role of Thermal Conductivity.* Small time temperature distributions during microwave heating in sinusoidal regime are shown in Figure 4 at $t = 0.1t_L$. Figure 4 illustrates the results for all the four

Table 3. $N_G$, $Bi$, $\mu_1$, $\mu_2$ and $t_L$ for Shrimp, Potato, Bread and Alumina Slabs in Sinusoidal Regime with $N_w = 0.5, 1, 1.5$ and $h_L = h_R = 2$ W m$^{-2}$ K$^{-1}$

| | Shrimp | | | Potato | | | Bread | | | Alumina | | |
|---|---|---|---|---|---|---|---|---|---|---|---|---|
| $N_w$ | 0.5 | 1.0 | 1.5 | 0.5 | 1.0 | 1.5 | 0.5 | 1.0 | 1.5 | 0.5 | 1.0 | 1.5 |
| $N_G$ | 0.806 | 1.612 | 2.420 | 0.590 | 1.181 | 1.771 | 2.770 | 5.540 | 8.300 | 0.036 | 0.072 | 0.107 |
| $Bi$ | 0.016 | 0.032 | 0.048 | 0.012 | 0.024 | 0.035 | 0.055 | 0.111 | 0.166 | 0.001 | 0.0014 | 0.002 |
| $\mu_1$ | 0.127 | 0.179 | 0.218 | 0.108 | 0.153 | 0.187 | 0.233 | 0.327 | 0.397 | 0.027 | 0.038 | 0.046 |
| $\mu_2$ | 1.581 | 1.591 | 1.601 | 1.578 | 1.586 | 1.593 | 1.605 | 1.638 | 1.670 | 1.571 | 1.5717 | 1.572 |
| $t_L/10^2$ (sec) | 0.33 | 1.29 | 2.87 | 0.297 | 1.177 | 2.625 | 3.05 | 11.71 | 25.36 | 0.053 | 0.212 | 0.48 |

materials corresponding to $N_w = 0.5$, 1 and 1.5, and $\phi_0 = 0$, 1/4 and 1/2. Note that the temperature distributions in Figure 4 are determined from Eq 4 using $h_L = h_R \equiv h = 2$ W m$^{-2}$ K$^{-1}$. Corresponding $N_G$, $Bi = hL/k$, $\mu_1$, $\mu_2$ and $t_L$ are reported in Table 3. In Figure 4, dimensionless temperature profiles are shown as $(\theta - 1) \times 10^2$ for shrimp, potato and bread, and $(\theta - 1) \times 10^4$ for Alumina. It may be noted that small time-temperature distributions for all the four materials follow the respective absorbed power distribution patterns shown in Figure 2. However, overall temperature gradients differ significantly from Alumina to bread with increasing temperature gradients in order from Alumina to potato, shrimp and bread. It may be further noted that, variations of $\theta(z)$ scale as $10^{-4}$ for Alumina, while they are of order $10^{-2}$ for shrimp, potato and bread. This is a direct consequence of the fact that temperature gradients within the material are proportional to $N_G$, which is inversely proportional to thermal conductivity. Since thermal conductivity of Alumina is much higher compared to other materials, $N_G$'s are orders of magnitude lower for Alumina and increase with potato, shrimp and bread for any fixed $N_w$ (see Table 3). This leads to corresponding increase of temperature gradients within the material. In addition, $N_G$ represents relative thermal diffusion time of a material (as discussed in the *Temperature distributions vs. power distributions* section), and materials with higher $N_G$ replicates the spatial oscillations of $q(z)$ much strongly in temperature distributions at fixed $t/t_L$. Thus, temperature distributions at $t = 0.1t_L$ exhibit much higher oscillations in bread, while the oscillations are gradually decayed in potato and shrimp. Finally, Alumina with $N_G \ll 1$ results in negligible spatial oscillations as shown in Figure 4.

Figure 5 illustrates small time-temperature distributions in exponential regime for $N_P = 3$, 4.5 and 6 and $\phi_0 = 0$, 1/4 and 1/2. The heat transfer coefficients in Figure 5 are assumed to be same as used in Figure 4 and corresponding $N_G$, $Bi$, $\mu_1$,

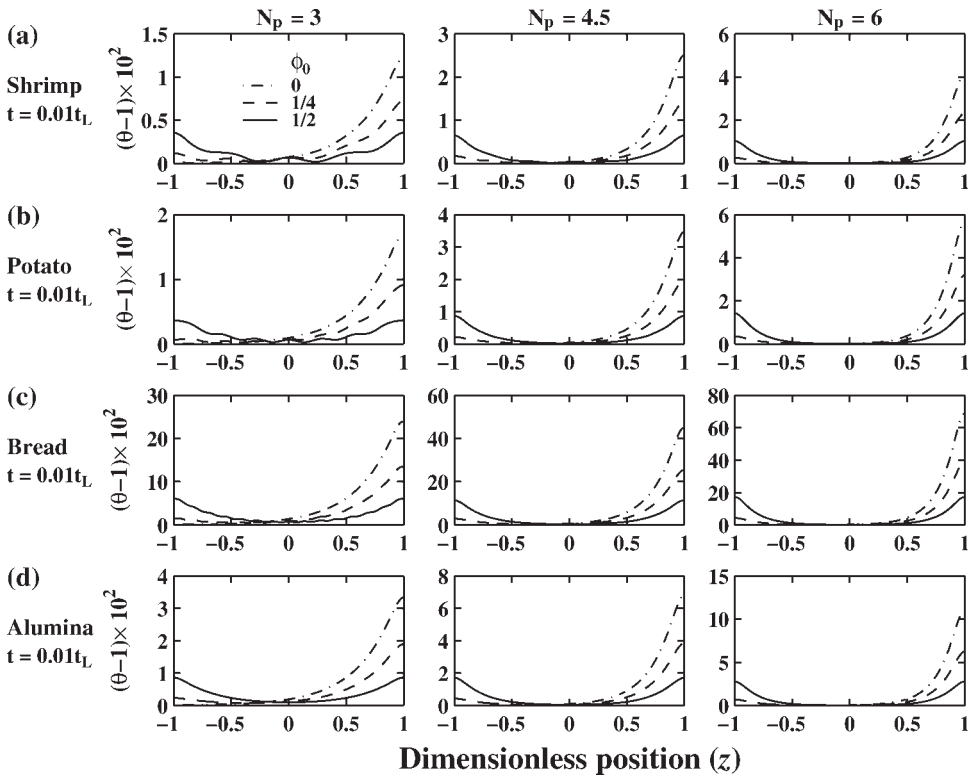


**Figure 5. Small time dimensionless temperature distributions ($(\theta - 1) \times 10^2$) in exponential regime of microwave heating of shrimp, potato, bread and Alumina.**

The results correspond to $t = 0.01t_L$, $h_L = h_R = 2$ W m$^{-2}$ K$^{-1}$, $N_p = 3$, 4 and 4.5, $\phi_0 = 0$ (dashed-dotted lines), 1/4 (dashed lines) and 1/2 (solid lines).

Table 4. $N_G$, $Bi$, $\mu_1$, $\mu_2$ and $t_L$ for Shrimp, Potato, Bread and Alumina Slabs in Exponential Regime with $N_p = 3, 4.5, 6$ and $h_L = h_R = 2$ W m$^{-2}$ K$^{-1}$

| | Shrimp | | | Potato | | | Bread | | | Alumina | | |
|---|---|---|---|---|---|---|---|---|---|---|---|---|
| $N_p$ | 3.0 | 4.5 | 6.0 | 3.0 | 4.5 | 6.0 | 3.0 | 4.5 | 6.0 | 3.0 | 4.5 | 6.0 |
| $N_G$ | 3.20 | 4.79 | 6.39 | 4.19 | 6.27 | 8.38 | 40.69 | 61.04 | 81.39 | 4.72 | 7.07 | 9.43 |
| $Bi$ | 0.064 | 0.096 | 0.128 | 0.084 | 0.126 | 0.168 | 0.814 | 1.221 | 1.628 | 0.094 | 0.142 | 0.189 |
| $\mu_1$ | 0.250 | 0.305 | 0.350 | 0.286 | 0.347 | 0.398 | 0.796 | 0.923 | 1.014 | 0.302 | 0.368 | 0.421 |
| $\mu_2$ | 1.611 | 1.630 | 1.648 | 1.622 | 1.647 | 1.671 | 1.964 | 2.098 | 2.206 | 1.627 | 1.656 | 1.682 |
| $t_L/10^2$ (sec) | 4.95 | 10.87 | 18.89 | 14.17 | 30.94 | 53.44 | 440.1 | 868.7 | 1396.1 | 855.1 | 1860.8 | 3205.0 |

$\mu_2$ and $t_L$ are listed in Table 4. Here, dimensionless temperature profiles as $(\theta - 1) \times 10^2$ are shown at $t = 0.01t_L$ for all the materials. It may be noted from Table 4 that for fixed $N_p$, bread has much higher $N_G$ compared to other three materials with shrimp, potato and Alumina having similar order of $N_G$. As a result, shrimp, potato and Alumina exhibit same order of temperature variations in exponential regime for fixed $N_p$. Whereas temperature variations within bread are much higher. However, temperature distributions in all the cases follow the absorbed power profiles shown in Figure 3.

The effect of boundary conditions on small time temperature distributions are shown in Figure 6 for three limiting cases of (a) both side insulated ($Bi_L = Bi_R = 10^{-3}$), (b) one side insulated and one side maintained at constant temperature ($Bi_L = 10^{-3}$, $Bi_R = 10^2$), and (c) constant temperatures at both sides ($Bi_L = Bi_R = 10^2$). Corresponding $\mu_2$ can be determined from Eq C2 given in Appendix C. Here, dimensionless temperature profiles scaled with $N_G$ given by $(\theta - 1) \times 10^2/N_G$ at $t = 0.1t_L$ are shown for shrimp with $N_w = 0.5$, 1, 1.5 and $\phi_0 = 0$, 1/4 and 1/2. Other materials also exhibit similar trends and are not shown here. It may be noted that the effects of boundary conditions are confined near the surfaces and small time temperature distributions within the slab follow the respective absorbed power profiles in all the cases (shown in Figure 2). The same is also true in exponential regime of power absorption as can be seen in Figure 6 for $\phi_0 = 0$ with $N_w = 1.5$, which corresponds to $N_p = 2.3$. It may also be noted that $(\theta - 1)/N_G$ exhibits similar order of magnitude for various $N_w$, since overall spatial gradients of temperature are proportional to $N_G$.

As discussed in the *Short time vs. long time* section, internal spatial oscillations of temperature distributions shown in Figures 4–6 tend to decay with time, and $\theta(z)$ approaches large time temperature distributions as $t \to t_L$. The threshold time not only depends on thermal properties, but also depends on slab length and boundary conditions. It may be noted that $t_L$ for a material increases with sample length and may become significantly high in exponential regime (see Table 4). Thus, large time heating in exponential regime might not be feasible for the materials selected here. It may be further noted from the magnitudes of $t_L$ reported

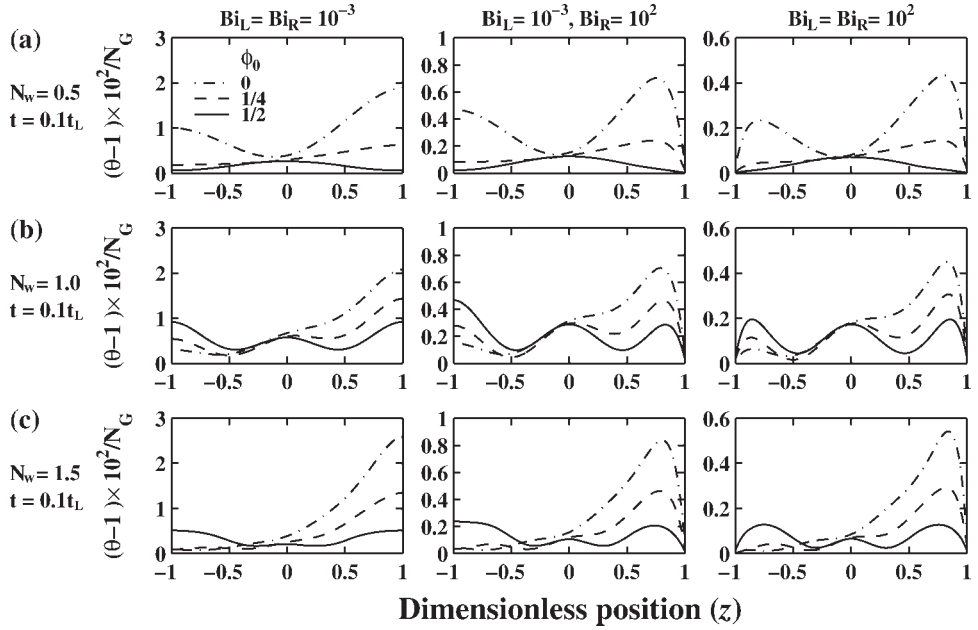


**Figure 6. Effect of boundary conditions on small time dimensionless temperature distributions ($(\theta - 1) \times 10^2/N_G$) for three limiting cases of (1) $Bi_L = Bi_R = 10^{-3}$, (2) $Bi_L = Bi_R = 10^2$, and (3) $Bi_L = 10^{-3}$, $Bi_R = 10^2$.**

The results are shown for shrimp with $N_w = 0.5$, 1, 1.5 and $\phi_0 = 0$ (dashed-dotted lines), 1/4 (dashed lines) and 1/2 (solid lines).

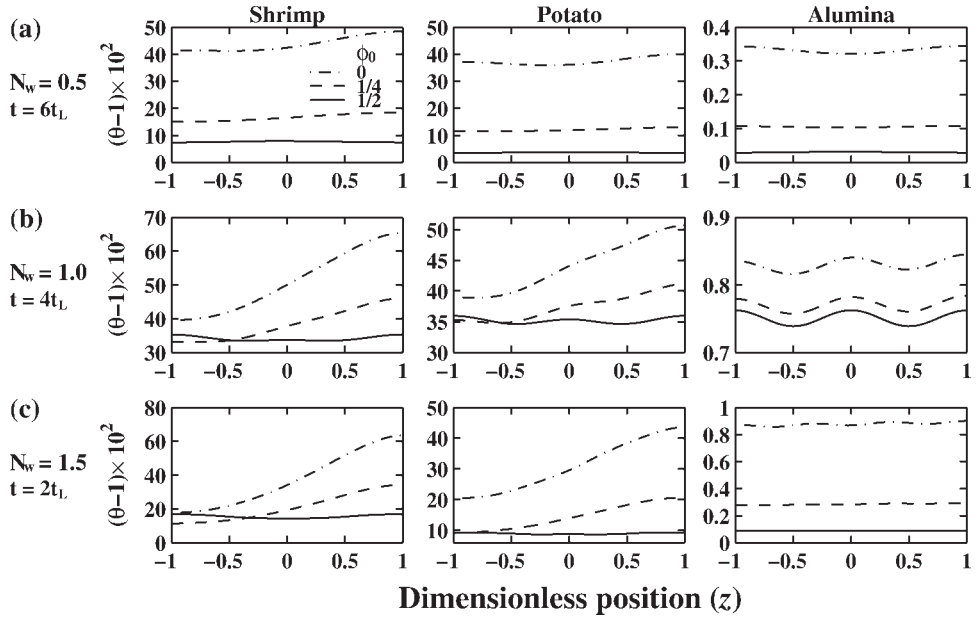


**Figure 7. Dimensionless temperature distributions ($(\theta - 1) \times 10^2$) for $Bi_L = Bi_R = 10^{-3}$ at various times within $1/\mu_2^2 < \tau < 1/\mu_1^2$.**

The results for shrimp, potato and Alumina with $\phi_0 = 0$, 1/4 and 1/2 are shown at $t = 6t_L$, $4t_L$ and $2t_L$ corresponding to $N_w = 0.5$, 1 and 1.5, respectively.

in Tables 3 and 4 that microwave heating of bread in both sinusoidal and exponential regimes will be confined to small time for most of the practical situations. Thus, large time heating patterns and their dependence on boundary conditions will be illustrated for shrimp, potato and Alumina in sinusoidal regime for three limiting cases of (1) $Bi_L = Bi_R = 10^{-3}$, (2) $Bi_L = Bi_R = 10^2$ and (3) $Bi_L = 10^{-3}$, $Bi_R = 10^2$.

*Large Time Temperature Distribution: Role of Biot Numbers.* Large time temperature distributions not only depend on the relative magnitudes of various eigenvalues, which determine $b_n$, but also depend on the absolute magnitude of first eigenvalue, which determines the spatial gradients of first eigenfunction. For $Bi_L$ and $Bi_R \ll 1$, $\mu_1 \rightarrow \sqrt{(Bi_L + Bi_R)/2}$ (see Eq. C1 of Appendix C), and the expression for large time temperature (Eq. 8) for $\tau < 1/\mu_1^2$ can be simplified to

$$\theta(z) - 1 = N_G \tau p_1 \psi_1(z) + N_G \sum_{n=2}^{\infty} \frac{p_n}{\mu_n^2} \psi_n(z), \quad \frac{1}{\mu_2^2} < \tau < \frac{1}{\mu_1^2} \tag{10}$$

In this case, the expression for $\mu_1$ (Eq. B4 with $n = 1$) simplifies to

$$\underset{Bi_L, Bi_R \rightarrow 0}{\psi_1(z)} = \frac{1}{\sqrt{2}} \cos\left[\sqrt{\frac{Bi_L + Bi_R}{2}}(1+z)\right] \approx \frac{1}{\sqrt{2}} \tag{11}$$

Thus, first eigenfunction becomes position invariant for small Biot numbers and spatial variations of higher order eigenfunctions are captured in Eq. 10 even though $\tau p_1$ is greater in magnitude. Therefore, following the discussion of small time temperature distributions, $\theta(z)$ for small Biot numbers follow the overall trend of absorbed power profiles till $\tau \ll 1/\mu_1^2$ as shown in Figure 7. In Figure 7, large time temperature variations for $Bi_L = Bi_R = 10^{-3}$ are shown for $N_w = 0.5$, 1 and 1.5 corresponding to $t = 6t_L$, $4t_L$ and $2t_L$, respectively. Since $t_L$ increases with $N_w$ and $Bi = 10^{-3}$ corresponds to almost no heat loss, the times at which temperature distributions are shown in Figure 7 are scaled to avoid extremely high-temperatures for higher $N_w$'s. It may be noted from Figure 7 that temperature distributions reflect the overall trend of $p(z)$. However, the internal oscillations of $p(z)$ are accordingly damped in temperature distributions based on $N_G$ (refer to Table 3 for various $N_G$).

The contribution of first term of Eq. 10 increases with time and becomes dominant as $\tau$ approaches $1/\mu_1^2$. Thus, large time temperature distributions for small Biot numbers mostly follow the first eigenfunction at $\tau \geq 1/\mu_1^2$. However, since $1/\mu_1^2$ is inversely proportional to Biot numbers, large time temperature distributions for $\{Bi_L, Bi_R\} << 1$ may not reach this stage in practice and follow absorbed power profile for the entire time. For small but finite Biot numbers, temperature distributions may reach the stage where first eigenfunction governs the large time temperature distributions as shown in Figure 8 for $Bi_L = Bi_R = 10^{-3}$, $10^{-2}$ and $10^{-1}$. Corresponding $\mu_1$ and $\mu_2$ can be determined from Eq. C1 and C2, and are listed in Table C.1. Here, large time temperature distributions at $t = 5t_L$, $10t_L$ and $20t_L$ are plotted for potato with $N_w = 0.5$ and $\phi_0 = 0$. Corresponding dimensionless times in terms of $1/\mu_1^2$ are reported in the figure and first eigenfunctions are shown on top of each case. It may be noted for Biot numbers of $10^{-3}$ and $10^{-2}$ that $\tau \ll 1/\mu_1^2$ for all the cases considered here and consequently temperature distributions follow $p(z)$ for the entire heating period. However, $\tau$ at $t = 20t_L$ ($\tau = 0.73/\mu_1^2$)

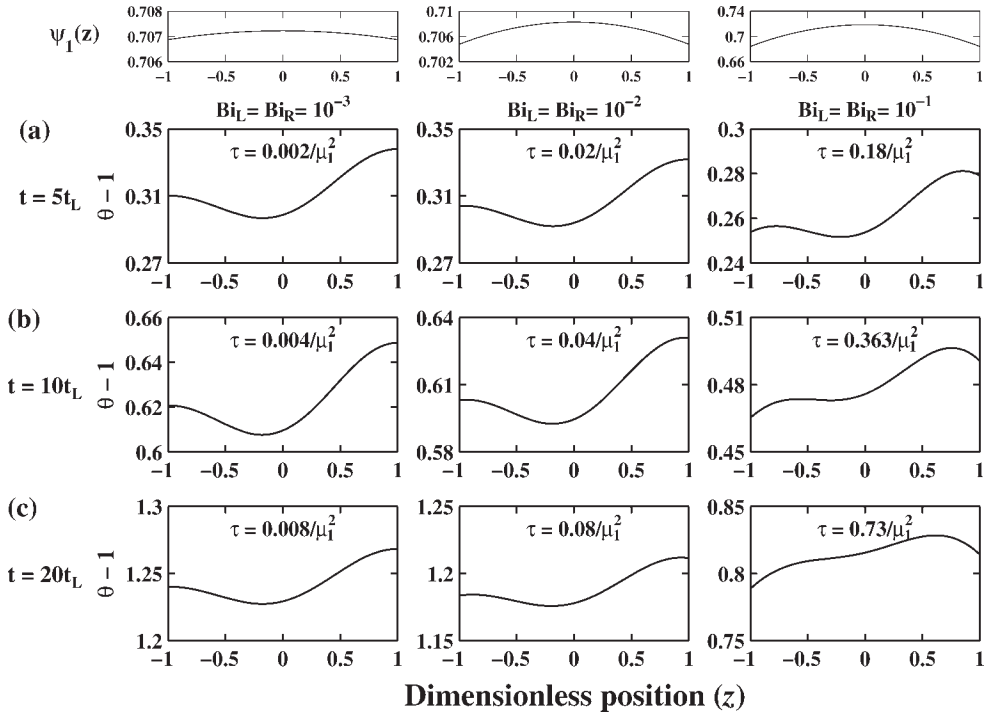


**Figure 8. Correspondence between temperature distributions at $\tau \rightarrow 1/\mu_1^2$, and the first eigenfunction profiles for small, but finite Biot numbers.**

Dimensionless temperature distributions ($\theta - 1$) at $t = 5t_L$, $10t_L$ and $20t_L$ are shown for potato with $Bi_L = Bi_R = 10^{-3}$, $10^{-2}$ and $10^{-1}$ and $\phi_0 = 0$.

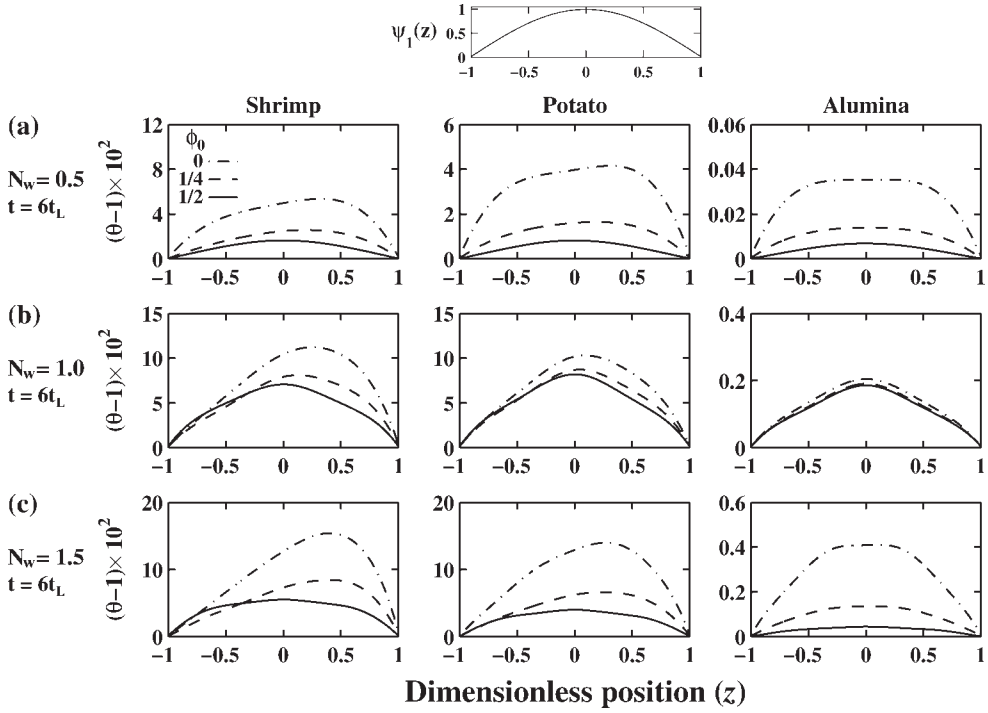


**Figure 9. Large time dimensionless temperature distributions ($(\theta - 1) \times 10^2$) in shrimp, potato and Alumina for large Biot numbers ($Bi_L = Bi_R = 10^2$).**

Dimensionless temperature distributions at $t = 6t_L$ are shown for $N_w = 0.5$, 1, 1.5 and $\phi_0 = 0$ (dashed-dotted lines), 1/4 (dashed lines) and 1/2 (solid lines).

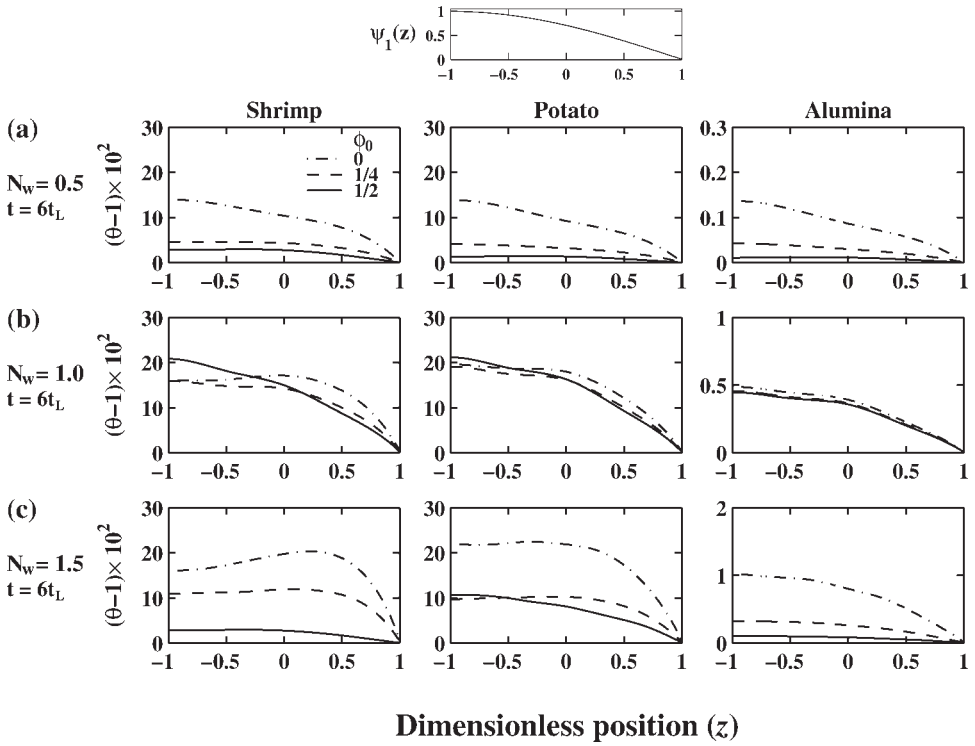


**Figure 10. Large time dimensionless temperature distributions ($(\theta - 1) \times 10^2$) in shrimp, potato and Alumina for $Bi_L = 10^{-3}$ and $Bi_R = 10^2$.**

Dimensionless temperature distributions at $t = 6t_L$ are shown for $N_w = 0.5$, 1, 1.5 and $\phi_0 = 0$ (dashed-dotted lines), 1/4 (dashed lines) and 1/2 (solid lines).

approaches $1/\mu_1^2$ for $Bi_L = Bi_R = 10^{-1}$, and the temperature distribution, which follows $p(z)$ at $t = 5t_L$ and $10t_L$, slowly evolves and approaches first eigenfunction at $t = 20t_L$.

For the other two cases of $\{Bi_L = 10^{-3}, Bi_R = 10^2\}$ and $Bi_L = Bi_R = 10^2$, $\mu_1 \to \pi/4$ and $\pi/2$, respectively (see Eq. C.1), and $\mu_2^2/\mu_1^2 \to 9$ and 4, respectively (see Appendix C), and first eigenfunction exhibits significant spatial variations. Thus, temperature distribution patterns follow the corresponding first eigenfunction and remain almost unchanged with time for $\tau > \tau_L$ as shown in Figures 9 and 10 for $\{Bi_L, Bi_R\} = 10^2$ and $\{Bi_L = 10^{-3}, Bi_R = 10^2\}$, respectively. In these figures, large time temperature distributions are shown at $t = 6t_L$ for shrimp, potato and Alumina corresponding to $N_w = 0.5$, 1 and 1.5 and $\phi_0 = 0$, 1/4 and 1/2. Corresponding first eigenfunctions are also shown on top of the figures. For all the cases, the temperature distribution patterns follow $\psi_1(z)$ irrespective of material and $\phi_0$.

### *Lump model*

Since Alumina satisfies $N_G \ll 1$ for $N_w = 0.5$, 1 and 1.5 (see Table 3), spatial temperature gradients become insignificant (see Figure 4), for these cases and evolution of temperature during both small and large time can be described by lump parameter model for all practical purposes. This is shown in Figure 11, which plots $\theta(z)$ at $t = 0.1t_L$, $10t_L$ and $100t_L$ for Alumina slabs with $N_w = 0.5$, 1 and 1.5. Here, the temperature distributions correspond to $h_L = h_R = 2$ W m$^{-2}$ K$^{-1}$. In Figure 11, symbols (○, □ and ◇ for $\phi_0 = 0$, 1/4 and 1/2, respectively) correspond to lump parameter model (Eq. 9), while lines (dashed-dotted, dashed and solid lines for $\phi_0 = 0$, 1/4 and 1/2, respectively) correspond to exact closed form solution (Eq. 4). It may be noted that temperature distributions can be well described by lump parameter model for large times, but exhibit deviations around the lump parameter model at $t = 0.1t_L$. However, the deviations are of order $N_G$, and, thus, lump parameter model can be used for prediction of temperature in both small and large times.

### *Discussions on* a priori *predictions*

This work is based on the scaling analysis of the closed form solution, which shows that heating patterns during microwave processing evolve in two stages. The heating characteristics and their governing factors in both the stages have been analyzed and illustrated for various materials, namely shrimp, potato, bread and Alumina. It has been shown that heating patterns in both the stages can be predicted based on two numbers, namely $N_G$ and $\tau_L$, where $N_G$ determines the overall temperature gradients within the material, and $\tau_L$ determines the threshold boundary between "small" and "large" time heating patterns. Temperature distributions during initial stages are slaved by imposed heat source profiles with temperature gradients proportional to $N_G$, and, consequently, spatial nonuniformities of microwave induced absorbed power initiate localized hot spots for $N_G \gg 1$. On the other hand, boundary conditions are more dominating factors during later stage of heating. Since $N_G$ and $\tau_L$ can be determined for a given material with known dimension and intensity of radiations, these two can

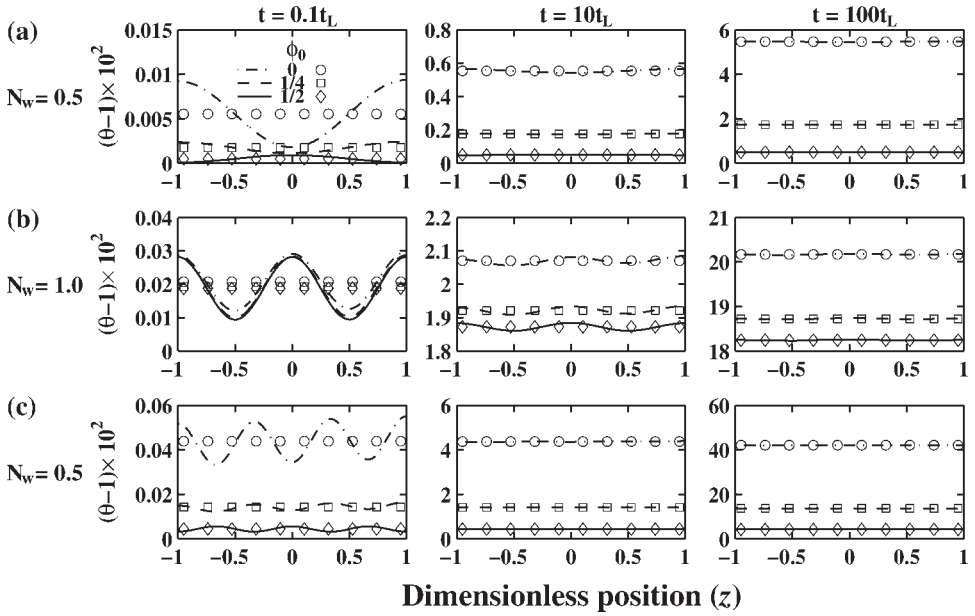


**Figure 11. Applicability of lump parameter model for small and large time heating of Alumina with $N_G \ll 1$.**

Dimensionless temperature distributions $(\theta - 1) \times 10^2$) for $N_w = 0.5$, 1, 1.5 and $\phi_0 = 0$ (dashed-dotted lines), 1/4 (dashed lines), 1/2 (solid lines) are shown at $t = 0.1t_L$, $10t_L$ and $100t_L$. Here, symbols represent lump parameter model, while lines correspond to Eq. 4.

can be used as guiding factors to predict the heating characteristics in a material.

The applicability of the present analysis is further illustrated by considering microwave processing of shrimp, potato, bread and Alumina slabs of length $2L = 2.5$ cm with $h_L = h_R = 2$ W m$^{-2}$ K$^{-1}$. Corresponding $N_G$, $Bi$, $\mu_1$, $\mu_2$ and $t_L$ are reported in Table 5. It may be noted from Table 5 that $N_G$ and $t_L$ are of similar order of magnitude for shrimp, potato and bread, while they are orders of magnitude smaller for Alumina. Therefore, based on present analysis it can be predicted from Table 5 that spatial profiles of absorbed power distributions will be closely reflected in bread slab of length 2.5 cm, while Alumina slab of same length will exhibit almost uniform temperature distributions. Temperature distributions within shrimp and potato will follow the respective absorbed power profiles, but internal oscillations will be damped in proportion to $N_G$. This is shown in Figure 12, which plots dimensionless temperature distributions, $(\theta - 1) \times 10^2$, within shrimp, potato, bread and Alumina slabs of length 2.5 cm. Here the temperature distributions for $\phi_0 = 0$, 1/4 and 1/2 are shown at $t = 30$ and 100 s, and corresponding absorbed power profiles are shown in subplots along first column. It may be noted that the temperature distributions are in accordance with the prediction. Also, in accordance with previous discussion the internal oscillations tend to die off with time, where materials with lower $N_G$ exhibit higher damping. Thus, $t_L$ and $N_G$ can be used for *a priori* prediction of hot spot initiations during microwave heating, since hot spots in microwave heating are mostly driven by nonuniformity of spatial power absorption. Lastly, Figure 12 illustrates the role of distributions of microwave source to tune the hot spot formation

## Conclusive Remarks

The objective of the present work is *a priori* prediction of heating dynamics in the presence of volumetric heat sources. A classic example of volumetric heating is experienced during the exposure of dielectrics to microwave radiations, where nonuniformities in spatial sources pose many challenging issues such as hot spot formation. This article is based on rigorous analysis of closed form solution of energy balance equation supplemented with microwave power absorption, where power absorption has been deduced via solving Helmholtz equation. Microwave power absorption is a very complex function of spatially distributed electric field, and, thus, the solution procedure requires a robust analysis. Such an analysis has been carried, out by Finite Fourier Transformation (FFT) for the first time to obtain the closed form solution for temperature field, which has been used to unfold some of the complex heating characteristics, based on one to one correspondence with power distributions.

**Table 5. $N_G$, $Bi$, $\mu_1$, $\mu_2$ and $t_L$ for Shrimp, Potato, Bread and Alumina Slabs of Length $2L = 2.5$ cm With $h_L = h_R = 2$ W m$^{-2}$ K$^{-1}$**

| | $N_G$ | $Bi$ | $\mu_1$ | $\mu_2$ | $t_L/10^2$ (*sec*) |
|---|---|---|---|---|---|
| **Shrimp** | 2.66 | 0.053 | 0.2286 | 1.6039 | 3.45 |
| **Potato** | 2.26 | 0.045 | 0.2108 | 1.5990 | 4.23 |
| **Bread** | 2.78 | 0.056 | 0.2335 | 1.6054 | 3.072 |
| **Alumina** | 0.05 | 0.001 | 0.0310 | 1.5714 | 0.096 |

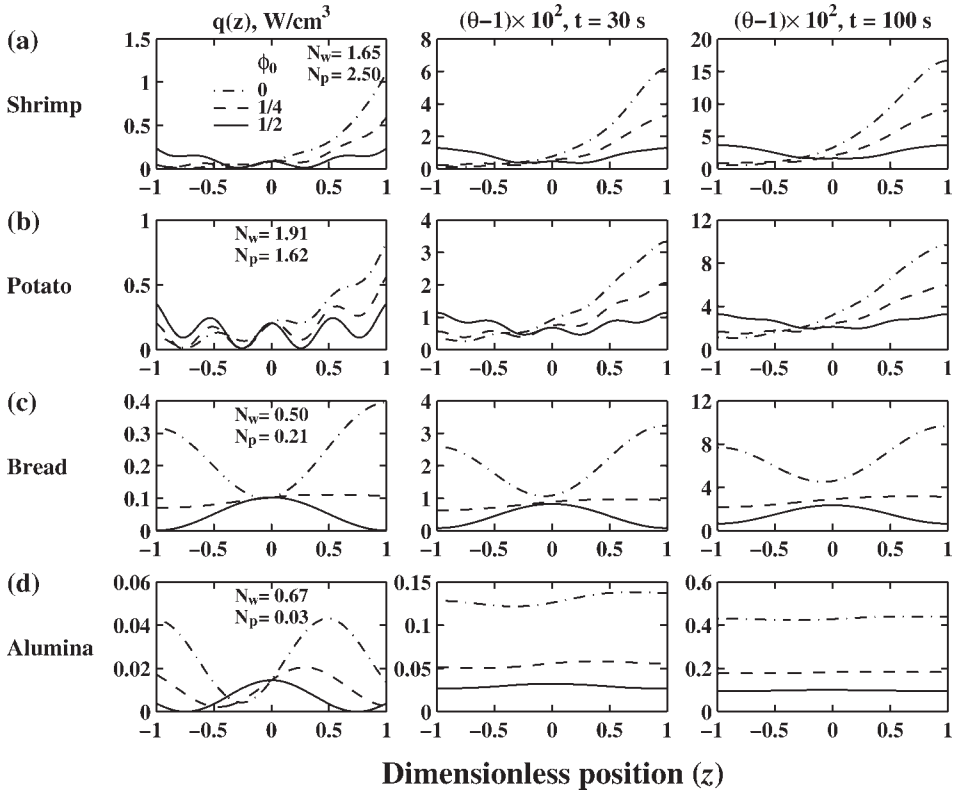


**Figure 12. Dimensionless temperature distributions ($(\theta - 1) \times 10^2$) at 30 and 100 s are shown within shrimp, potato, bread and Alumina slabs of length 2.5 cm.**

Here, 1st column shows corresponding absorbed power distributions.

Current closed form analysis establishes time scales "short or long" along with suitability of distributed or lump parameter models. The time scales and hot spots are useful to estimate optimal sample thicknesses and processing strategies, based on time or distribution of microwave incidence. These estimates will be further useful to analyze the complex heating characteristics associated with drying, melting, chemical reactions, material processing with temperature dependent dielectric properties etc., where the closed form analysis may not be possible.

This investigation presents a comprehensive theoretical understanding on various microwave heating characteristics. Although a number of experimental observations[11–13] on temperature distributions exist for thick samples, experimental data exhibiting other heating characteristics of samples within resonating regime in presence of uniform plane wave have not been reported yet. Solution of Helmholtz equation reduces to Lambert's law in the limit of thick samples, and our closed form solution does predict the experimental trend in thick sample regime. The verifications for other length scales will be possible in future, subject to the availability of experimental investigations in those regimes.

## Acknowledgment

Authors would like to thank the anonymous reviewer for the critical comments which are helpful to improve the quality of the manuscript.

## Notation

$Bi_L(Bi_R)$ = left(right) side Biot number
$c$ = velocity of light, m $s^{-1}$
$C_p$ = specific heat capacity, J $kg^{-1}$ $K^{-1}$
$D_p$ = penetration depth within material, m
$E_0$ = total incident electric field, V $m^{-1}$
$E_{x,m}(E_{x,0})$ = induced electric field within material(free space), V $m^{-1}$
$E_L(E_R)$ = incident electric field from left(right) side, V $m^{-1}$
$f$ = frequency of incident radiation, Hz
$h_L(h_R)$ = left(right) side heat-transfer coefficient, W $m^{-2}$ $K^{-1}$
$I_L(I_R)$ = flux of incident radiation from left(right) side, W $m^{-2}$
$k$ = thermal conductivity, W $m^{-1}$ $K^{-1}$
$L$ = half length of the slab, m
$q(z')$ = absorbed power distribution, W $m^{-3}$
$p(z)$ = dimensionless absorbed power distribution
$p_n$ = power Fourier coefficient ($\langle p(z), \psi_n(z) \rangle$)
$N_w(N_p)$ = wave(penetration) number of a material
$N_{w,0}$ = wave number of free space
$T$ = temperature, K
$T_0(T_\infty)$ = initial(ambient) temperature, K
$t_L$ = threshold time between small and large time heating, sec
$\tau_L$ = dimensionless threshold time between small and large time heating

### *Greek letters*

$\alpha$ = thermal diffusion time, sec
$\mu_n(\psi_n)$ = $n$th eigenvalue(eigenfunction)
$\phi_0$ = fractional incident electric field from left side
$\rho$ = density, kg $m^{-3}$
$\theta$ = dimensionless temperature
$\theta_0(\theta_\infty)$ = dimensionless initial(ambient) temperature
$\varepsilon_0$ = free space permittivity, Farad $m^{-1}$

$\lambda_m(\lambda_0)$ = wavelength within material(free space), m
$\kappa'(\kappa'')$ = dielectric constant(loss) of the material

## Literature Cited


1. Ayappa KG, Davis HT, Crapiste G, Davis EA, Gordon J. Microwave-heating - an evaluation of power formulations. *Chem Eng Sci*. 1991;46(4):1005.
2. Ayappa KG, Davis HT, Davis EA, Gordon J. 2-Dimensional finite-element analysis of microwave-heating. *AIChE J*. 1992;38(10): 1577.
3. Ratanadecho P, Aoki K, Akahori M. A numerical and experimental study of microwave drying using a rectangular wave guide. *Drying Technol*. 2001;19(9):2209.
4. Ratanadecho P, Aoki K, Akahori M. The characteristics of microwave melting of frozen packed beds using a rectangular waveguide. *IEEE Transac On Microwave Theory and Techniques*. 2002;50(6): 1495.
5. Basak T, Ayappa KG. Analysis of microwave thawing of slabs with effective heat capacity method. *AIChE J*. 1997;43(7):1662.
6. Bhattacharya M, Basak T, Ayappa KG. A fixed-grid finite element based enthalpy formulation for generalized phase change problems: role of superficial mushy region. *Intl J of Heat and Mass Transfer*. 2002;45(24):4881–4898.
7. Liu F, Turner I, Bialkowski M. A finite-difference time-domain simulation of power-density distribution in a dielectric-loaded microwave cavity. *J of Microwave Power and Electromagnetic Energy*. 1994;29(3):138–148.
8. Liu F, Turner I, Siores E, Groombridge P. A numerical and experimental investigation of the microwave heating of polymer materials inside a ridge waveguide. *J of Microwave Power and Electromagnetic Energy*. 1996;31(2):71–82.
9. Zhang Q, Jackson TH, Ungan A, Gao D. Numerical modeling of continuous hybrid heating of cryo-preserved tissue. *Intl J of Heat and Mass Transfer*. 1999;42(3):395–403.
10. Zhang QO, Jackson TH, Ungan A. Numerical modeling of microwave induced natural convection. *Intl J of Heat and Mass Transfer*. 2000;43(12):2141–2154.
11. Mao WJ, Watanabe M, Sakai N. Analysis of temperature distributions in Kamaboko during microwave heating. *J of Food Eng*. 2005;71(2):187–192.
12. Campanone LA, Zaritzky NE. Mathematical analysis of microwave heating process. *J of Food Eng*. 2005;69(3):359–368.
13. Taher BJ, Farid MM. Cyclic microwave thawing of frozen meat: experimental and theoretical investigation. *Chem Eng and Processing*. 2001;40(4):379–389.
14. Ayappa KG, Davis HT, Barringer SA, Davis EA. Resonant microwave power absorption in slabs and cylinders. *AIChE J*. 1997; 43(3):615.
15. Barringer SA, Ayappa KG, Davis EA, Davis HT, Gordon J. Power absorption during microwave-heating of emulsions and layered systems. *J Food Sci*. 1995;60(5):1132.
16. Basak T. Generalized analysis on microwave-assisted material processing for one-dimensional slabs: Metallic support versus free space. *Ind Eng Chem Res*. 2005;44(9):3075.
17. Basak T, Kumaran SS. A generalized analysis on material invariant characteristics for microwave heating of slabs. *Chem Eng Sci*. 2005; 60(20):5480.
18. Basak T. Role of resonances on microwave heating of oil-water emulsions. *AIChE J*. 2004;50(11):2659.
19. Marchant TR, Pincombe AH. Microwave-heating of materials with temperature-dependent wavespeed. *Wave Motion*. 1994;19(1):67.
20. Marchant TR. Microwave-heating of materials with impurities. *J Eng Math*. 1994;28(5):379.
21. Andonowati A, Chandra D. The effect of spatial inhomogeneity in thermal conductivity on the formation of hot-spots. *J Eng Math*. 2000;38(2):101.
22. Ward MJ. Thermal runaway and microwave heating in thin cylindrical domains. *IMA J App Math*. 2002;67(2):177.
23. Reimbert CG, Jorge MC, Minzoni AA, Vargas CA. A note on caustics and two-dimensional hot spots in microwave heating. *J Eng Math*. 2002;44(2):147–153.
24. Yang HW, Gunasekaran S. Temperature profiles in a cylindrical model food during pulsed microwave heating. *J Food Sci*. 2001; 66(7):998.
25. Vriezinga CA, Sanchez-Pedreno S, Grasman J. Thermal runaway in microwave heating: a mathematical analysis. *Appl Math Modeling*. 2002;26(11):1029.
26. Lee MZC, Marchant TR. Microwave thawing of cylinders. *Appl Math Modelling*. 2004;28(8):711.
27. Basak T. Analysis of resonances during microwave thawing of slabs. *Int J Heat Mass Transfer*. 2003;46(22), 4279.
28. Basak T, Priya AS. Role of ceramic supports on microwave heating of materials. *J Appl Physics*. 2005;97(8):Art. No. 083537.
29. Basak T. Influence of various shapes of annular metallic support on microwave heating of 2D cylinders. *Chem Eng Sci*. 2006;61(6): 2023.
30. Bejan A. *Convection Heat Transfer*. 3rd ed. John Wiley & Sons, Hoboken, NJ; 2004.
31. Bhattacharya M, Basak T. Detailed material-invariant analysis on spatial resonances of power absorption for microwave-assisted material processing with distributed sources. *Ind Eng Chem Res*. 2007; 46(3):750.
32. Bhattacharya M, Basak T. A novel closed form analysis on asymptotes and resonances of microwave power. *Chem Eng Sci*. 2006;61(19):6273.
33. Oliveira ME, Franca AS. Microwave heating of foodstuffs. *J Food Eng*. 2002;53:347.
34. Yildiz A, Palazoglu K, Erdogdu F. Determination of heat and mass transfer parameters during frying of potato slices. *J Food Eng*. 2007;79(1):11.
35. Barringer SA, Davis EA, Gordon J, Ayappa KG, Davis HT. Microwave-heating temperature profiles for thin slabs compared to Maxwell and Lambert law predictions. *J Food Eng*. 1995;60: 2659.
36. Bird RB, Stewart WE, Lightfoot EN. *Transport Phenomena*. John Wiley & Sons, New York; 1994.
37. Carslaw HS, Jaeger JC. *Conduction of Heat in Solids*. Calendron Press, Oxford; 1959.


## Appendix

### *A. Power absorption due to microwave radiations*

Dipolar interactions with electromagnetic fields results in power absorption ($q(z')$) within a dielectric exposed to microwave radiations, where the extent of interactions depends on dielectric constant ($\kappa'_m$), and dielectric loss ($\kappa''_m$) of the material. The absorbed power within the material acts as volumetric heat sources and is related to the induced electric field ($E_{x,m}(z')$) as

$$q(z') = \pi f \epsilon_0 \kappa''_m E_{x,m}(z') E^*_{x,m}(z') \tag{A1}$$

where $E_{x,m}(z')$ can be obtained by solving the following Helmholtz equations within the material and surrounding medium along with associated interfacial conditions

$$\frac{d^2E_{x,m}}{dz'^2} + \frac{4\pi^2 f^2}{c^2}\left(\kappa'_m + i\kappa''_m\right)E_{x,m} = 0, \quad -L \le z' \le L \tag{A2a}$$

$$\frac{d^2E_{x,0}}{dz'^2} + \frac{4\pi^2 f^2}{c^2}E_{x,0} = 0, \quad -L < z' \text{ and } z' > L \tag{A2b}$$

$$E_{x,0} = E_x, \quad \frac{dE_{x,0}}{dz'} = \frac{dE_x}{dz'} \quad \text{at } z' = \pm L. \tag{A2c}$$

In the aforementioned equations, superscript * denotes the complex conjugate, $E_{x,0}$ is the induced electric field within free space on left and right sides, $\varepsilon_0$ is the free space permittivity, $f$ is the frequency of incident radiation, and $c$ is the velocity of light.

In terms of wave number ($N_w = 2L/\lambda_m$), penetration number ($N_p = 2L/D_p$), and wave number for the free space ($N_{w,0}$

$= 2L/\lambda_0$), where $\lambda_m$ and $D_p$ are the wavelength and penetration depth within the material, and $\lambda_0$ is the wavelength within free space, solution of Eq. A2 can be written as

$$E_{x,m} = T_m e^{(i\pi N_w - N_p/2)z} + R_m e^{(N_p/2 - i\pi N_w)z} \tag{A3a}$$

$$E_{x,0} = T_j e^{i\pi N_{w,0} z} + R_j e^{-i\pi N_{w,0} z} \quad j = \begin{cases} L & z < -1 \\ R & z > 1 \end{cases} \tag{A3b}$$

The wavelength and penetration depth within a material depend on the dielectric properties as given below

$$\lambda_m = \frac{c\sqrt{2}}{f\left[\sqrt{\kappa_m'^2 + \kappa_m''^2} + \kappa_m'\right]^{1/2}}, \tag{A4a}$$

and

$$D_p = \frac{c}{\sqrt{2}\pi f\left[\sqrt{\kappa_m'^2 + \kappa_m''^2} - \kappa_m'\right]^{1/2}} \tag{A4b}$$

and $\lambda_0$ is given by

$$\lambda_0 = \frac{c}{f}. \tag{A4c}$$

In Eq. A3, $z = z'/L$, $T_l$ and $R_l$ ($l = m, L, R$) are coefficients of transmission and reflection, respectively, with

$$T_L = E_L \equiv \sqrt{\frac{2I_L}{c\epsilon_0}}, \quad R_R = E_R \equiv \sqrt{\frac{2I_R}{c\epsilon_0}} \tag{A5}$$

Here, $E_L$ and $E_R$ are the corresponding incident electric fields due to incident radiation fluxes of $I_L$ and $I_R$ from left and right sides, respectively.[18,27,31]

Solving $R_L$, $T_m$, $R_m$ and $T_R$ from Eq. A2c, dimensionless volumetric heat source distribution $p(z) = q(z')/q_0$ can be written as

$$p(z) = \frac{N_w N_p}{N_{w,0} C_d}\left[C_{n,1}\cosh N_p z + C_{n,2}\sinh N_p z + \sqrt{C_{n,3}^2 + C_{n,4}^2}\sin\left(2\pi N_w z + \gamma\right)\right] \tag{A6}$$

where $q_0 = c\varepsilon_0 E_0^2/2L$, $E_0 = E_L + E_R$ is the total incident electric field

$$C_d = \frac{c_3^2 - c_1^2}{8\pi^4 N_{w,0}^4}\cos 4\pi N_w + \frac{c_2^2 + c_4^2}{8\pi^4 N_{w,0}^4}\cosh 2N_p + \frac{N_p c_1}{2\pi N_{w,0}}\sin 4\pi N_w + \frac{N_w c_2}{N_{w,0}}\sinh 2N_p, \tag{A7a}$$

$$C_{n,1} = 2\phi_0(1-\phi_0)\sqrt{c_1^2 + c_3^2}\cos(2\pi N_w - \gamma_1) + \left(1 - 2\phi_0 + 2\phi_0^2\right)\left(c_2\cosh N_p + c_4\sinh N_p\right) \tag{A7b}$$

$$C_{n,2} = (1-2\phi_0)\left(c_2\sinh N_p + c_4\cosh N_p\right), \tag{A7c}$$

$$C_{n,3} = \left(1 + 2\phi_0^2 - 2\phi_0\right)\sqrt{c_1^2 + c_3^2}\cos(2\pi N_w - \gamma_1) + 2\phi_0(1-\phi_0)\left(c_2\cosh N_p + c_4\sinh N_p\right) \tag{A7d}$$

$$C_{n,4} = -(1-2\phi_0)\sqrt{c_1^2 + c_3^2}\sin(2\pi N_w - \gamma_1) \tag{A7e}$$

$$\gamma = \text{sign}\left(C_{n,3}\right)\cos^{-1}\frac{C_{n,4}}{\sqrt{C_{n,3}^2 + C_{n,4}^2}} \tag{A7f}$$

$$\gamma_1 = -\cos^{-1}\frac{c_1}{\sqrt{c_1^2 + c_3^2}} \tag{A7g}$$

In the previous expressions, $\phi_0 = E_L/E_0$ is the fractional incident electric field from left side and $c_1 - c_4$ are defined as

$$c_1 = 2\pi^2 N_{w,0}^2\left(\pi^2 N_w^2 + N_p^2/4 - \pi^2 N_{w,0}^2\right) \tag{A8a}$$

$$c_2 = 2\pi^2 N_{w,0}^2\left(\pi^2 N_w^2 + N_p^2/4 + \pi^2 N_{w,0}^2\right) \tag{A8b}$$

$$c_3 = -2\pi^3 N_{w,0}^3 N_p, \tag{A8c}$$

$$c_4 = 4\pi^4 N_{w,0}^3 N_w. \tag{A8d}$$

### *B. Closed form solution by Finite Fourier Transformation*

In Finite Fourier Transformation, $\theta$ is expressed as a combination of orthonormal set of eigenfunction such that

$$\theta = \sum_{n=1}^{\infty}\theta_n(\tau)\psi_n(z); \quad \theta_n = \langle\theta, \psi_n\rangle \tag{B1}$$

where $\psi_n$ satisfies the following eigenvalue problem associated with Eq. 3

$$\frac{d^2\psi_n}{dz^2} = -\mu_n^2\psi_n; \quad -1 \le z \le 1 \tag{B2a}$$

$$\frac{d\psi_n}{\partial z} = Bi_L\psi_n \quad @\ z = -1 \tag{B2b}$$

$$-\frac{d\psi_n}{\partial z} = Bi_R\psi_n \quad @ =\ z = 1 \tag{B2c}$$

Here, the orthonormality condition is given by

$$\langle\psi_m, \psi_n\rangle = \int_{-1}^{1}\psi_m(z)\psi_n(z)dz = \delta_{mn} \tag{B3}$$

where $\delta_{mn}$ is Krönecker delta.

Solving Eq. B2, eigenfunctions can be written as

$$\psi_n = \frac{Bi_L\sin\mu_n(1+z) + \mu_n\cos\mu_n(1+z)}{\sqrt{\mu_n^2 + Bi_L^2}\sqrt{1 + \frac{\left(\mu_n^2 + Bi_L Bi_R\right)\sin 4\mu_n}{4\mu_n\left(\mu_n^2 - Bi_L Bi_R\right)}}}, \quad n = 1, 2....\infty \tag{B4}$$

where eigenvalues satisfy the following characteristic equation

**Table C1. $\mu_1$ and $\mu_2$ for Various $Bi_L$ and $Bi_R$**

| | $\mu_1$ | | | | | | $\mu_2$ | | | | | |
|---|---|---|---|---|---|---|---|---|---|---|---|---|
| $Bi_L$ or $Bi_R$ | 0.001 | 0.01 | 0.1 | 1 | 10 | 100 | 0.001 | 0.01 | 0.1 | 1 | 10 | 100 |
| 0.001 | 0.032 | | | | | | 1.571 | | | | | |
| | 0.032 | | | | | | 1.571 | | | | | |
| 0.01 | 0.074 | 0.100 | | | | | 1.574 | 1.577 | | | | |
| | 0.074 | 0.100 | | | | | 1.574 | 1.577 | | | | |
| 0.1 | 0.218 | 0.228 | 0.3111 | | | | 1.602 | 1.605 | 1.632 | | | |
| | 0.218 | 0.228 | 0.311 | | | | 1.602 | 1.605 | 1.633 | | | |
| 1.0 | 0.539 | 0.545 | 0.599 | 0.860 | | | 1.822 | 1.824 | 1.846 | 2.029 | | |
| | 0.534 | 0.540 | 0.594 | 0.864 | | | 1.857 | 1.859 | 1.882 | 2.078 | | |
| 10.0 | 0.749 | 0.754 | 0.807 | 1.100 | 1.429 | | 2.246 | 2.248 | 2.267 | 2.432 | 2.863 | |
| | 0.749 | 0.754 | 0.807 | 1.182 | 1.429 | | 2.245 | 2.248 | 2.265 | 2.437 | 2.859 | |
| 100.0 | 0.782 | 0.788 | 0.840 | 1.140 | 1.489 | 1.555 | 2.345 | 2.347 | 2.366 | 2.532 | 2.982 | 3.111 |
| | 0.782 | 0.788 | 0.840 | 1.178 | 1.489 | 1.555 | 2.345 | 2.347 | 2.366 | 2.538 | 2.978 | 3.110 |

$$\tan 2\mu_n = \frac{\mu_n(Bi_L + Bi_R)}{\mu_n^2 - Bi_L Bi_R}, \quad n = 1, 2....\infty \tag{B5}$$

Taking inner product of Eq. 3a with $\psi_n$ according to Eq. B3, and integrating by parts, $\theta_n$ is obtained as

$$\theta_n(\tau) = \langle 1, \psi_n(z)\rangle\left(1 + (\theta_0 - 1)e^{-\mu_n^2\tau}\right) + N_G\frac{\left(1 - e^{-\mu_n^2\tau}\right)}{\mu_n^2}\langle p(z), \psi_n(z)\rangle \tag{B6}$$

where

$$\langle 1, \psi_n\rangle = \frac{Bi_L + \frac{\mu_n^2 + Bi_L^2}{\mu_n^2 - Bi_L Bi_R} Bi_R \cos 2\mu_n}{\mu_n\sqrt{\mu_n^2 + Bi_L^2}\sqrt{1 + \frac{\left(\mu_n^2 + Bi_L Bi_R\right)\sin 4\mu_n}{4\mu_n\left(\mu_n^2 - Bi_L Bi_R\right)}}} \tag{B7a}$$

and

$$\begin{aligned}\langle p, \psi_n\rangle \equiv p_n = {} & \frac{N_w N_p}{N_{w,0} C_d\sqrt{\mu_n^2 + Bi_L^2}\sqrt{1 + \frac{\left(\mu_n^2 + Bi_L Bi_R\right)\sin 4\mu_n}{4\mu_n\left(\mu_n^2 - Bi_L Bi_R\right)}}} \\ & \times\Bigg[\frac{\cosh N_p}{\mu_n^2 + N_p^2}\Big(\left(\mu_n^2 C_{n,1} + Bi_L C_{n,2} N_p\right)\sin 2\mu_n \\ & + \mu_n\Big(Bi_L C_{n,1} - C_{n,2} N_p\Big)2\sin^2\mu_n\Big) \\ & + \frac{\sinh N_p}{\mu_n^2 + N_p^2}\Big(\left(\mu_n^2 C_{n,2} + Bi_L C_{n,1} N_p\right)\sin 2\mu_n \\ & + \mu_n\left(C_{n,1} N_p - Bi_L C_{n,2}\right)2\cos^2\mu_n\Big) + \frac{\sqrt{C_{n,3}^2 + C_{n,4}^2}}{\mu_n^2 - 4\pi^2 N_w^2} \\ & \times\Big(2\pi N_w(\mu_n\cos 2\mu_n + Bi_L\sin 2\mu_n)\cos(\gamma + 2\pi N_w) \\ & \times\ \mu_n\big[Bi_L\sin(\gamma - 2\pi N_w) - 2\pi N_w\cos(\gamma - 2\pi N_w) \\ & + (\mu_n\sin 2\mu_n - Bi_L\cos 2\mu_n)\sin(\gamma + 2\pi N_w)\big]\Big)\Bigg]\end{aligned} \tag{B7b}$$

Thus, evolution of temperature distribution within the slab with internal heat generation $p(z)$ can be determined from the following expression (obtained from Eq. B1)

$$\theta = 1 + \sum_{n=1}^{\infty}\left[\langle 1, \psi_n(z)\rangle(\theta_0 - 1)e^{-\mu_n^2\tau} + N_G\frac{\left(1 - e^{-\mu_n^2\tau}\right)}{\mu_n^2}\langle p(z), \psi_n(z)\rangle\right]\psi_n(z) \tag{B8}$$

by finding $\mu_n$ as $n$th root of Eq. B5. Theoretically, evaluation of $\theta$ involves summation of an infinite series, which in turn requires the determination of a large number of roots of the eigen equation (Eq. B5). However, due to monotonically increasing nature of eigenvalues (i.e., $\mu_{i+1} > \mu_i\ \forall i$) the infinite series in Eq. B8 converges for finite number terms.

### C. Asymptotic expressions for first and second eigenvalues

The eigenvalue problem given by Eq. B2 is not only relevant to the present problem, but also appears in variety of problems involving unsteady or convective diffusion of heat or mass.[36,37] In such problems, first two eigenvalues provide important insight about various time scales associated with different stages of evolution as discussed in *Temperature distributions vs. power distributions* section. Since, eigenvalues vary with Biot numbers, closed expressions for $\mu_1$ and $\mu_2$ are necessary for the prediction of the time scales. Asymptotic analysis of Eq. B5 reveals that there exist three different asymptotes of $\mu_1$ and $\mu_2$, which can be obtained via asymptotic expansion, and are written as

$$\mu_1 = \begin{cases}\sqrt{\frac{Bi_L + Bi_R + 2Bi_L Bi_R}{2 + Bi_L + Bi_R}}\left(1 - \frac{Bi_L + Bi_R}{12} + \frac{11(Bi_L + Bi_R)^2}{1440}\right) & \{Bi_L, Bi_R\} \le 1 \\ \frac{\pi}{2} - \frac{\pi}{4}\left(\frac{1}{Bi_L} + \frac{1}{Bi_R}\right) + \frac{\pi}{8}\left(\frac{1}{Bi_L} + \frac{1}{Bi_R}\right)^2 & \{Bi_L, Bi_R\} > 1 \\ \frac{\pi}{4} + \frac{2Bi_i}{\pi} - \frac{\pi}{8Bi_j} - \frac{16Bi_i^2}{\pi^3} + \frac{\pi}{16Bi_j^2}; & \{i,j\} = L \text{ and } R,\quad Bi_i\langle 1, Bi_j\rangle 1\end{cases} \tag{C1}$$

and

$$\mu_2 = \begin{cases}\frac{\pi}{2} + \frac{(Bi_L + Bi_R)}{\pi} - \frac{2(Bi_L + Bi_R)^2}{\pi^3}; & \{Bi_L, Bi_R\} \le 1 \\ \pi - \frac{\pi}{2}\left(\frac{1}{Bi_L} + \frac{1}{Bi_R}\right) + \frac{\pi}{4}\left(\frac{1}{Bi_L} + \frac{1}{Bi_R}\right)^2 & \{Bi_L, Bi_R\} > 1 \\ \frac{3\pi}{4} + \frac{2Bi_i}{3\pi} - \frac{3\pi}{8Bi_j} - \frac{16Bi_i^2}{27\pi^3} + \frac{3\pi}{16Bi_j^2}; & \{i,j\} = L \text{ and } R,\quad Bi_i < 1, Bi_j > 1\end{cases} \tag{C2}$$

Thus, $\mu_1$ varies from $\sqrt{(Bi_L + Bi_R)/2}$ to $\pi/4$ as $Bi_L$ varies from 0 to $\infty$ with $Bi_R \ll 1$ (or vice versa), and from $\pi/4$ to $\pi/2$ as $Bi_L$ varies from 0 to $\infty$ with $Bi_R \gg 1$ (or vice versa). Similarly, $\mu_2$ varies from $\pi/2$ to $3\pi/4$ as $Bi_L$ varies from 0 to $\infty$ with $Bi_R \ll 1$ (or vice versa) and from $3\pi/4$ to $\pi$ as $Bi_L$ varies from 0 to $\infty$ with $Bi_R \gg 1$ (or vice versa). For finite $Bi_L$ and $Bi_R$, $\mu_1$ and $\mu_2$ are confined within the aforementioned asymptotic band, and can be predicted from the earlier expressions as shown in Table C1. In this table, the prediction of the above asymptotes (Eqs. C1 and C2) are compared with the exact value corresponding to the first root of Eq. B5. For each Biot number in Table C1, the first row corresponds to Eq. B5, while the second row corresponds to Eq. C1 or C2. It may be noted that these asymptotes predict the eigenvalues with very high-accuracy.

*Manuscript received Mar. 19, 2007, and revision received Sept. 14, 2007.*